

Numerical simulations of wormlike micelles flows in micro-fluidic T-shaped junctions

M. Colin, T. Colin^a, J. Dambrine^b

^a*Mc2, INRIA Bordeaux Sud-Ouest, Institut de Mathématiques de Bordeaux (UMR 5251)
Université Bordeaux 1, 351 cours de la Libération - F 33405 Talence Cedex*

^b*Laboratoire de Mathématiques et Applications (UMR 6086) Téléport 2 - BP 30179
Boulevard Marie et Pierre Curie 86962 Futuroscope Chasseneuil Cedex*

Abstract

Numerical simulations of non-newtonian fluids such as wormlike micellar solutions in confined geometries are of great interest in the oil industry. Their main property called shear-banding is a brutal transition from a very viscous state to a very fluid state above a certain threshold value of shear stress. This feature leads to a very complex behavior in 3D flows.

A modified version of the Johnson-Segalman's model, adapted to our situation (flows with a strong extensional component) is presented. A particular attention is paid to inlet and outlet boundary conditions, and a Poiseuille-like submodel is derived in order to get natural velocity and stress profiles that can be used at the boundaries. A numerical method is then developed, and stability issues are presented.

Our results show the interest of the modified Johnson-Segalman's model performed in this article. A set of 3D numerical simulations are then presented in order to understand the influence of the junction geometry upon the jamming effects observed in the behaviour of this kind of fluids.

Keywords: Rheology, Wormlike micelles, Microfluidics, Shear banding, T-Junctions, Jamming effects, 3D simulations

1. Introduction

1.1. General context

This paper presents some numerical analysis and simulations on a model used to describe the non-newtonian behavior of wormlike micelles solutions. Wormlike micelles are polymer-like microscopic structures, that can break

and reform permanently (for this reason micelles are often referred as "living polymers"). According to its very singular non-newtonian properties, worm-like micelles are used in many fields of the industry from food processing to oil recovery [14].

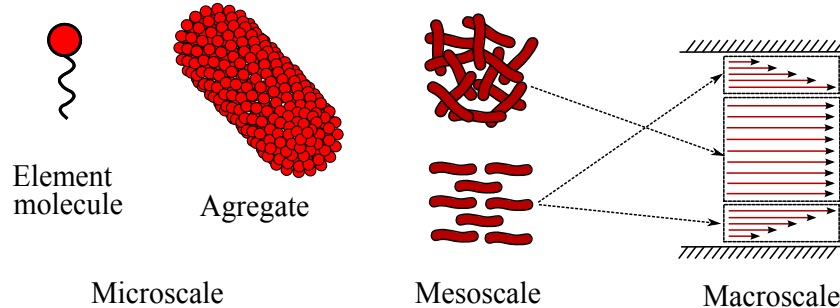


Figure 1: Flow of a wormlike micellar solution, from the micro-scale to the macro-scale

Numerical simulations in non-newtonian fluid dynamics yield many challenging issues (see [20] as a review of numerical problems encountered in this field), the most notable problem being the so-called "high Weissenberg number problem" (see [10] [11]). Since fluids such as wormlike micelles do not allow situations in which elastic effects are too large (above a critical shear stress the behavior of the fluid becomes close to newtonian), the high Weissenberg number problem doesn't occur here. However, many other issues arise in our case, such as extensional instabilities and the choice of appropriate boundary conditions.

Our study will focus on oil recovery applications. Usually, micro-fluidic networks serve as simplified experimental models to understand percolation and drainage in porous media (see [24] for a review of the subject). In the following work, we focus on the case of a T-shaped junction, as an element of a more complex network. The geometry considered here is depicted on figure 2. In simulations, the fluid is injected through the boundary Γ_3 and exits through Γ_1 and Γ_2 . The walls are denoted Γ_w . The expected phenomenon here is the jamming of one branch of the junction for some values of the inlet flow rate (as observed in [17]). This phenomenon can be explained, in some extent, by the particular shear rheology of the fluid.

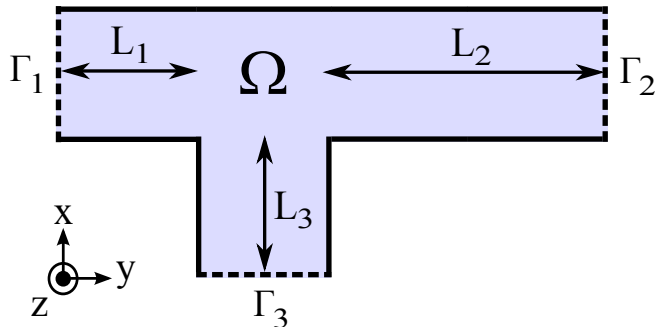


Figure 2: Schematic view and notations for the T-shaped domain

The main rheological feature of wormlike micelles is "shear-banding", which can be defined as the capacity of a fluid to separate into phases of different viscosities when exposed to a shear stress [18]. For wormlike micelles, the micro-structural interpretation of shear-banding is the following: at rest, the micelles are in an entangled state, but when a sufficiently high shear stress is applied they align quickly in the flow direction. As a consequence, when the applied shear stress is non-homogeneous (like in a pipe flow), high shear rate bands are formed in the area of high shear stress (see Figure 1), leading to plug flows, as observed also with yield stress fluids. An experimental work that shows this phenomenon can be found in [16].

A particular model has been shown relevant for the description of flows of wormlike micellar solutions: the Johnson-Segalman model introduced in [13] (see [5] for a complete review of models for wormlike micelles, and more recently [26]). The originality of this model is that, under a constant shear rate, it allows a non-monotonic relation between the shear rate and the shear stress (Figure 3). However, in a real hydrodynamic context (shear rate given by a momentum equation) the necessary monotonicity of the shear rate / shear stress relation leads to the selection of a stress plateau. This stress plateau is history-dependent and some hysteresis on this model has been shown in literature [1]. The addition of a diffusion term in the model allows the selection of a unique stress plateau (for physical interpretation of this term see [8]).

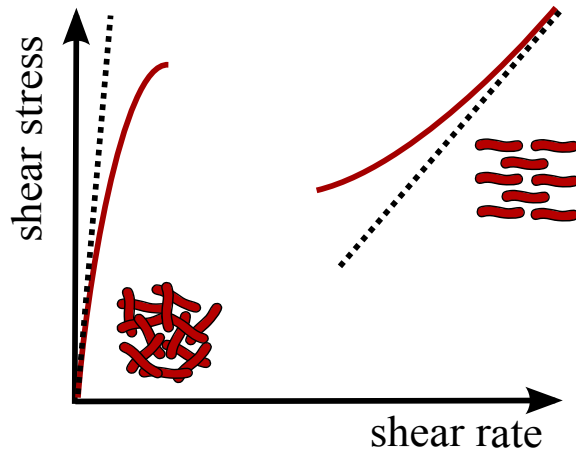


Figure 3: Typical flow curve of the Johnson-Segalman model

1.2. The main difficulties

Despite the fact that it has become a standard model for wormlike micelles, the Johnson-Segalman model (as many linear models) is not adapted when one wants to deal with extensional flows. Such models are valid in the limit of small extensional rates. Recall that our aim is to study the flow through a T-shaped junction and that flows in such a geometry exhibit strong extensional rates. In order to counterbalance this effect, among a lot of possibilities, we chose to add a quadratic term in the constitutive equation (see [12]).

Some issues concerning the appropriate boundary conditions to be set at $\Gamma_{1,2,3}$ are also discussed through the following article. First, concerning inlet boundary conditions the problem is that typical inlet velocity profiles are, in our case, much different from the classical Poiseuille profile (derived from the Stokes model without non-newtonian extra-stress). By assuming a parallel invariant flow along one direction in the full 3D system, we derived a Poiseuille-like model for non-newtonian fluids that succeeded in retrieving the typical "plug-flow" profile observed in experiments. For outlet conditions the problem is much more delicate, the constraint being that the inlet flow rate must equal the sum of the outlet flow rates. Still, there is an infinity of "plug-flow" profiles that fulfill this requirement. Two approaches were studied. The first, based on simplifying hypothesis, allowed us to compute an appropriate set outlet velocities. The other approach is based on "free flow" boundary conditions.

1.3. Outline of the paper

In Section 2, we present our model : governing equations and models for boundary conditions. First, in Section 2.1 the Johnson-Segalman constitutive equation is introduced. We present the advantages and the drawbacks of this model through simplified situations (fixed homogeneous shear stress, fixed extensional rate). This lead us to a modification of the initial constitutive equation, presented in Section 2.1.2. The derivation of the Poiseuille-like model mentioned above is then presented in Section 2.1.3.

Once the model is known, a numerical scheme based on finite difference methods is developed in Section 3. This scheme relies on an explicit coupling between the momentum equation and the constitutive equation. It is expected that such an explicit coupling should induce instabilities if the time step is not chosen carefully. For this reason an analysis of stability is performed in Section 3.4. First, linear stability is proved on the continuous model, and then a necessary stability condition on the time step is determined.

The Section 4 details all the numerical results obtained with the model and the numerical methods mentioned above. In order to validate our model, we investigate in Section 4.1 two cases: a strong extensional flow in a cross slot domain, and the micro-fluidic junction used in experiments. Both cases will illustrate the necessity of a non-linearity in the constitutive equation. Then, the non-standard behavior observed on wormlike micelles flows for a strongly asymmetrical junction is shown through numerical simulations. Finally we investigate the sensitivity of outlet flow rates distribution to the asymmetry of the junction.

2. Problem setting

Let us consider a domain Ω describing a T-shaped micro-fluidic junction (see Figure 2).

2.1. Governing Equations

The fluid described here is supposed to be incompressible. Moreover, the low dimensions involved in micro-fluidics ($\sim 100\mu m$) usually leads to very low Reynolds number flows. Therefore, it is commonly admitted that the Stokes model is appropriate in this context:

$$\nabla \cdot \mathbf{T} = \nabla P, \tag{2.1}$$

$$\nabla \cdot \mathbf{V} = 0, \tag{2.2}$$

where \mathbf{T} represents the fluid stress tensor, P the pressure and $\mathbf{V} = (u, v, w)$ the velocity. Considering a Jeffrey fluid, the stress tensor \mathbf{T} reads:

$$\mathbf{T} = 2\eta\mathbf{D} + \boldsymbol{\Sigma}, \quad (2.3)$$

where η represents a characteristic viscosity of the fluid (commonly referred as the "solvent viscosity"), \mathbf{D} the Cauchy's strain tensor, and $\boldsymbol{\Sigma}$ the extra stress tensor. In order to close the system, one needs to give an equation on $\boldsymbol{\Sigma}$. Several possibilities exist, we chose to study the Johnson-Segalman constitutive law, which is one of the most adapted for shear banding fluids.

2.1.1. The Johnson-Segalman constitutive equation

The diffusive Johnson-Segalman model [13] reads:

$$\overset{\diamond}{\boldsymbol{\Sigma}} = 2G\mathbf{D} - \frac{1}{\tau}\boldsymbol{\Sigma} + \mathcal{D}\Delta\boldsymbol{\Sigma}, \quad (2.4)$$

where G is an elastic modulus, τ a characteristic local relaxation time, and \mathcal{D} a diffusion coefficient. Thanks to the diffusion term introduced in [8], the hysteretic behavior of the original model is suppressed. The symbol \diamond represents the Gordon-Showalter time derivative of the stress tensor $\boldsymbol{\Sigma}$:

$$\overset{\diamond}{\boldsymbol{\Sigma}} = (\partial_t + \mathbf{V} \cdot \nabla)\boldsymbol{\Sigma} - (\boldsymbol{\Omega}\boldsymbol{\Sigma} - \boldsymbol{\Sigma}\boldsymbol{\Omega}) - a(\mathbf{D}\boldsymbol{\Sigma} + \boldsymbol{\Sigma}\mathbf{D}) \quad (2.5)$$

where:

$$\mathbf{D} = \frac{\nabla\mathbf{V} + \nabla\mathbf{V}^t}{2},$$

$$\boldsymbol{\Omega} = \frac{\nabla\mathbf{V} - \nabla\mathbf{V}^t}{2}.$$

The full model hence reads :

$$\left\{ \begin{array}{l} \nabla \cdot (2\eta\mathbf{D} + \boldsymbol{\Sigma}) = \nabla P, \\ \nabla \cdot \mathbf{V} = 0, \\ \overset{\diamond}{\boldsymbol{\Sigma}} = 2G\mathbf{D} - \frac{1}{\tau}\boldsymbol{\Sigma} + \mathcal{D}\Delta\boldsymbol{\Sigma}. \end{array} \right. \quad (2.6)$$

This model has been used extensively in literature for the description of wormlike micelles flows ([19] [9]), mostly for its interesting behavior in the particular case of shear flows. Let us now discuss the pertinence of the model (2.6) with the study of two particular situations : the shear flow and the extensional flow.

The homogeneous shear flow.

In this first study, we consider an unidirectional shear flow, invariant along x . The strain hence writes :

$$\nabla \mathbf{V} = \begin{pmatrix} 0 & 0 & \dot{\gamma} \\ 0 & 0 & 0 \\ 0 & 0 & 0 \end{pmatrix}. \quad (2.7)$$

Moreover, the stress is supposed to be homogeneous. By plugging the strain (2.7), and the above hypotheses into the full model, one can prove that the system (2.6) reduces to :

$$\begin{cases} \eta \dot{\gamma} + \sigma^{xy} = T_a^{xy}, \\ \partial_t \sigma^* = 2(a^2 - 1) \dot{\gamma} \sigma^{xy} - \frac{1}{\tau} \sigma^*, \\ \partial_t \sigma^{xy} = \frac{1}{2} \dot{\gamma} \sigma^* - \frac{1}{\tau} \sigma^{xy} + G \dot{\gamma}, \end{cases} \quad (2.8)$$

where $\sigma^* = (a - 1) \sigma^{xx} + (a + 1) \sigma^{yy}$, and T_a^{xy} is the (given) applied shear stress. In the following, we consider two situations : a slowly increasing shear stress ($T_a^{xy}(t) = \beta t$ with $\beta \ll G/\tau$) and a slowly decreasing shear stress ($T_a^{xy}(t) = T^{max} - \beta t$ with $\beta \ll G/\tau$).

As we can see on Figure 4, the values of the shear stress/strain are distributed on two different branches : the low shear rate branch, which corresponds to a high viscosity and the high shear rate branch which corresponds to a low viscosity. If the shear stress is raised above a certain threshold value, the shear rate jumps up. Similarly, if we decrease the shear stress underneath an other threshold value, the shear rate jumps down. In an heterogeneous situation, this threshold behavior leads to the coexistence of two phases (fluid/viscous) within the same fluid. This phenomenon is often referred as "shear-banding". Despite this interesting behavior in a shear flow, it can be shown that the Johnson-Segalman model is not relevant for the description of an extensional flow, as shown in the following situation.

The homogeneous extensional flow.

Let us consider the following extensional flow:

$$\nabla \mathbf{V} = \begin{pmatrix} 2\dot{\epsilon} & 0 & 0 \\ 0 & -\dot{\epsilon} & 0 \\ 0 & 0 & -\dot{\epsilon} \end{pmatrix}.$$

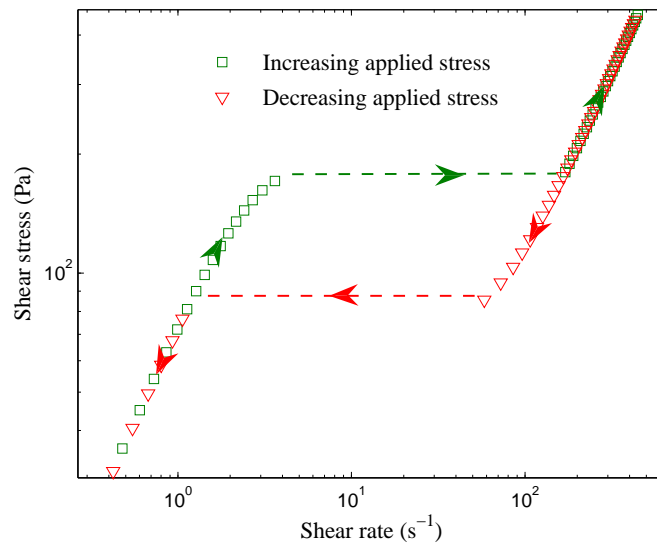


Figure 4: Rheological curves obtained on the model (2.8) for the following set of parameters: $G = 150 Pa$, $\tau = 0.5 s$, $\eta = 1 Pa.s$, $a = 0.9$. The squares represent the shear stress/strain relation for the increasing T_a^{xy} , and the triangles represent the shear stress/strain relation for the decreasing T_a^{xy} . Dashed lines : stress thresholds.

where $\dot{\epsilon}$ is the extension rate (supposed constant and known). If we suppose the stress and strain to be homogeneous, the system (2.6) becomes:

$$\begin{cases} \partial_t \sigma^{xx} = \left(2a\dot{\epsilon} - \frac{1}{\tau}\right) \sigma^{xx} + 2G\dot{\epsilon}, \\ \partial_t \sigma^{yy} = -\left(a\dot{\epsilon} + \frac{1}{\tau}\right) \sigma^{yy} - G\dot{\epsilon}, \\ \partial_t \sigma^{zz} = -\left(a\dot{\epsilon} + \frac{1}{\tau}\right) \sigma^{zz} - G\dot{\epsilon}, \end{cases} \quad (2.9)$$

We hence deduce the steady states for the first normal stress:

$$\sigma^{xx}(\dot{\epsilon}) = 2G\tau \frac{\dot{\epsilon}}{1 - 2a\tau\dot{\epsilon}}.$$

From the first equation in (2.9) and (2.10) it is clear that the model doesn't admit a steady state for $\dot{\epsilon} = (2a\tau)^{-1}$. In fact all the steady states for $\dot{\epsilon} > (2a\tau)^{-1}$ are unstable steady states since the value of the "growth rate" of σ^{xx} ((2.9), first equation) is positive for these values of $\dot{\epsilon}$. As a consequence, no steady state can be reached for the first normal stress above a certain value of the extension rate. This infinite growth of the first normal stress above a critical value of the extension rate is a well known unphysical behavior, which is commonly attributed to the very linear nature of the model. A modification of the model is hence performed in the following section.

Note that one could argue that supposing a steady homogeneous strain is not realistic, and that effects of the feedback of the extra-stress on the strain via the momentum equation could suppress this non-physical behavior. In section 4.1.1 we show some numerical simulations that the instability shown here persists even without the hypothesis mentioned above.

2.1.2. The non linear model

Following the approach of Giesekus [12], we add a second order non-linearity to the system:

$$\dot{\Sigma} = 2G\mathbf{D} - \frac{1}{\tau}\Sigma - \frac{\kappa}{G\tau}\Sigma^2 + \mathcal{D}\Delta\Sigma, \quad (2.10)$$

where κ is a dimensionless number to be taken between 0 and 0.5. Again, we investigate the behavior of this model in the case of an homogeneous

extensional flow. In this particular case the model (2.10) reduces to:

$$\begin{cases} \partial_t \sigma^{xx} = \left(2a\dot{\epsilon} - \frac{1}{\tau}\right) \sigma^{xx} - \frac{\kappa}{G\tau} (\sigma^{xx})^2 + 2G\dot{\epsilon}, \\ \partial_t \sigma^{yy} = -\left(a\dot{\epsilon} + \frac{1}{\tau}\right) \sigma^{yy} - \frac{\kappa}{G\tau} (\sigma^{yy})^2 - G\dot{\epsilon}, \\ \partial_t \sigma^{zz} = -\left(a\dot{\epsilon} + \frac{1}{\tau}\right) \sigma^{zz} - \frac{\kappa}{G\tau} (\sigma^{zz})^2 - G\dot{\epsilon}, \end{cases} \quad (2.11)$$

The steady states of the model are defined for all $\dot{\epsilon}$, and it can be proved easily that they are all stable. The Figure 5 (squares) shows these steady states computed for various values of the extension rate. We notice that the singular behavior observed for the linear model (circles) is suppressed here. The steady stress/strain relation is asymptotically linear and the slope of this asymptote corresponds to a limit extensional viscosity which is higher than the viscosity at rest. This behavior is quite satisfactory. We compare both models in Section 4.1 in some "real" configurations, that is, when the rate of deformation is given by the solution of a momentum equation, instead of a fixed given value, as here. Finally, the full model studied in this paper reads:

$$\begin{cases} \nabla \cdot (2\eta \mathbf{D} + \boldsymbol{\Sigma}) = \nabla P, \\ \nabla \cdot \mathbf{V} = 0, \\ \overset{\circ}{\boldsymbol{\Sigma}} = 2G\mathbf{D} - \frac{1}{\tau}\boldsymbol{\Sigma} - \frac{\kappa}{G\tau}\boldsymbol{\Sigma}^2 + \mathcal{D}\Delta\boldsymbol{\Sigma}. \end{cases} \quad (2.12)$$

Since we are interested in realistic situations, that is we deal with a bounded domain, we need to introduce suitable boundary conditions to System 2.12. In literature, very few results are available, in particular concerning shear-banding fluids. One of the main interest of this article is to bring to the fore appropriate boundary conditions for the inlet/outlet flow. For that purpose we introduce a very useful sub-model of (2.12): the "Poiseuille-like" model.

2.1.3. A Poiseuille-like model

In this section we consider a sub-model of (2.12). In the spirit of [7], the aim here is to describe a flow through a straight infinite channel along the x direction (for instance) upon which a pressure drop δP is applied. In such a situation it is known that the following hypothesis can be made. We let the

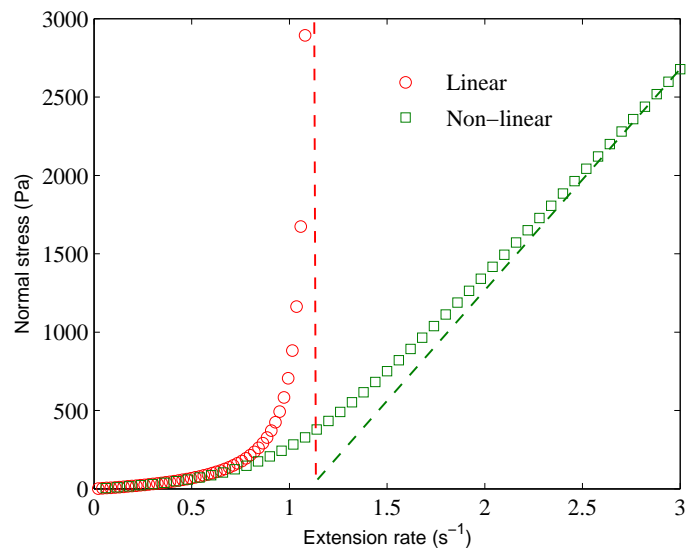


Figure 5: Normal stress / extension rate relations obtained on the model (2.8) for the following set of parameters: $G = 150 \text{ Pa}$, $\tau = 0.5 \text{ s}$, $\eta = 1 \text{ Pa}\cdot\text{s}$, $a = 0.9$. The circles represent the stress/strain relation for the linear model, and the rectangles represent the stress/strain relation for the non-linear model ($\kappa = 0.1$). Dashed lines : asymptotes.

flow to be unidirectional along x :

$$\mathbf{V} = \begin{pmatrix} u \\ 0 \\ 0 \end{pmatrix}, \quad (2.13)$$

and that the velocity and stress tensor are invariant along x :

$$\partial_x u = 0, \quad (2.14)$$

$$\partial_x \boldsymbol{\Sigma} = 0. \quad (2.15)$$

By plugging (2.13), (2.14) and (2.15) into (2.12), we obtain the 2D Poiseuille-like model:

$$\begin{cases} 2\eta \Delta_{yz} u + \partial_y \Sigma^{xy} + \partial_z \Sigma^{xy} = \delta P, \\ \overset{\circ}{\boldsymbol{\Sigma}} = 2G \mathbf{D} - \frac{1}{\tau} \boldsymbol{\Sigma} - \frac{\kappa}{G\tau} \boldsymbol{\Sigma}^2 + \mathcal{D} \Delta \boldsymbol{\Sigma}. \end{cases} \quad (2.16)$$

Note that, in this case the strain tensor has a much simpler expression:

$$\nabla \mathbf{V} = \partial_y u (\boldsymbol{\delta}_{i,j}^{1,2})_{0 \leq i,j \leq 3} + \partial_z u (\boldsymbol{\delta}_{i,j}^{1,3})_{0 \leq i,j \leq 3},$$

$(\boldsymbol{\delta}_{i,j}^{1,2})_{0 \leq i,j \leq 3}$ (r.p. $(\boldsymbol{\delta}_{i,j}^{1,3})_{0 \leq i,j \leq 3}$) being the matrix having only 0 entries except on the first row, second column (r.p. third column), for which the value is 1.

The main interest of the model (2.16) is that it reproduces the typical velocity profile for the Johnson-Segalman fluid in a straight channel. As a consequence, the profile obtained by solving the system (2.16) at steady state (see Figure 6) is a good candidate for an inlet/outlet boundary condition. Moreover, the only input data here is the inlet pressure gradient δP , which is often accessible in experiments. Note that the system (2.16) is a 2D system so the cost of computing this velocity profile is rather small (in our 3D context).

2.2. Boundary conditions

One of the main issues when dealing with micro-fluidic flow simulations is the setting of appropriate inlet conditions (Γ_3). For instance, in our case, the typical velocity profiles are very different from standard Poiseuille profiles (see Figure 6). In order to deal with this difficulty, we first solve numerically the submodel (2.16). In practice the solution always reaches a stationary state, which is denoted in the sequel $\mathbf{V}^{\delta P}(y, z) = (u^{\delta P}(y, z), 0, 0)$ and $\boldsymbol{\Sigma}^{\delta P}(y, z)$. Then our choice is to set at the inlet:

$$\begin{aligned} \mathbf{V}|_{\Gamma_3} &= \mathbf{V}^{\delta P}(y, z), \\ \boldsymbol{\Sigma}|_{\Gamma_3} &= \boldsymbol{\Sigma}^{\delta P}(y, z). \end{aligned}$$

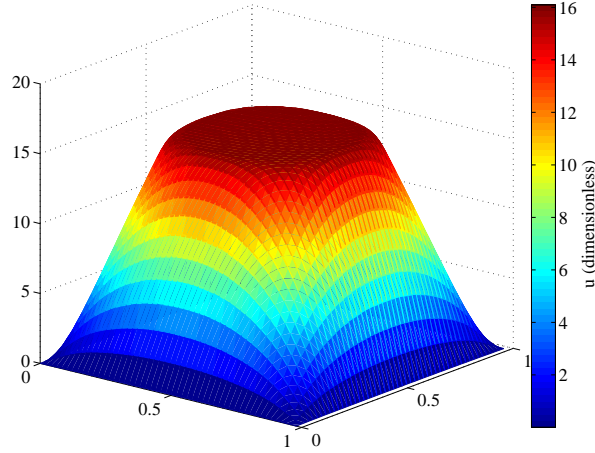


Figure 6: Typical inlet velocity profile obtained by solving numerically the sub-model (2.16) at steady-state

Note that, by this procedure, we indirectly set the inlet pressure gradient.

Concerning the outlet (Γ_1 and Γ_2), the situation is a bit delicate. Two different situations are introduced here. In the first one, we used the stationary solution of the Poiseuille-like model (2.16) in order to prescribe the outlet velocity and stress profiles through Γ_1 and Γ_2 . It is important to notice that the input parameters δP_1 and δP_2 have to be well chosen in this case, since we need to ensure the incompressibility condition:

$$\int_{\Gamma_3} \mathbf{V}^{\delta P_3} \cdot \vec{n} = \int_{\Gamma_1} \mathbf{V}^{\delta P_1} \cdot \vec{n} + \int_{\Gamma_2} \mathbf{V}^{\delta P_2} \cdot \vec{n}.$$

In the second situation, we use classical Neumann boundary conditions as follows:

$$\partial_{\vec{n}} \mathbf{V}|_{\Gamma_{1,2}} = 0, \quad (2.17)$$

$$\partial_{\vec{n}} \Sigma|_{\Gamma_{1,2}} = 0. \quad (2.18)$$

The comparison between the two outlet boundary conditions described above is discussed through numerical simulations in section 4.2.

It remains to set the conditions on the walls Γ_w for both \mathbf{V} and Σ . In the context of micro-fluidics, it is still an open question. Some experiments

performed in [16] suggested that the chemical nature of the surface as well as its roughness could have an important influence on the flow. In this paper we focused on the following boundary conditions:

$$\mathbf{V}|_{\Gamma_w} = 0, \quad (2.19)$$

$$\partial_{\bar{n}}\boldsymbol{\Sigma}|_{\Gamma_w} = 0. \quad (2.20)$$

The Dirichlet condition on the velocity (2.19) is a no-slip boundary condition. The Neumann boundary condition upon the stress tensor (2.20) components implies that the extra-stress does not induce any tangential force at the vicinity of the walls. As a consequence, below the critical regime from which shear banding occurs, some "apparent slip" is observed, even though a no-slip condition is set for the velocity.

3. Discretization of the equations

In this section, we introduce our numerical scheme. As already explained, our aim is to perform 3D numerical experiments. Let us first recall the full model (2.12):

$$\nabla \cdot (2\eta \mathbf{D} + \boldsymbol{\Sigma}) = \nabla P, \quad (3.21)$$

$$\nabla \cdot \mathbf{V} = 0, \quad (3.22)$$

$$\partial_t \boldsymbol{\Sigma} + \mathbf{V} \cdot \nabla \mathbf{V} - f_a(\boldsymbol{\Sigma}, \nabla \mathbf{V}) = 2G \mathbf{D} - \frac{1}{\tau} \boldsymbol{\Sigma} - \frac{\kappa}{G\tau} \boldsymbol{\Sigma}^2 + \mathcal{D}\Delta \boldsymbol{\Sigma}. \quad (3.23)$$

For simplicity, in equation (3.23) we denote by $f_a(\boldsymbol{\Sigma}, \nabla \mathbf{V})$ the Gordon-Schowalter objective derivative terms:

$$f_a(\boldsymbol{\Sigma}, \nabla \mathbf{V}) = (\boldsymbol{\Omega} \boldsymbol{\Sigma} - \boldsymbol{\Sigma} \boldsymbol{\Omega}) + a(\mathbf{D} \boldsymbol{\Sigma} + \boldsymbol{\Sigma} \mathbf{D}).$$

Note that, for a given strain $\nabla \mathbf{V}$, f_a is linear with respect to $\boldsymbol{\Sigma}$.

3.1. Semi discretization in time

Let δt be the time step, and $t_n = n\delta t$ the discretized time, where $n \in \mathbb{N}$. Let us also denote by $\mathbf{V}^n(x, y, z)$ the velocity computed at time t^n , and $\boldsymbol{\Sigma}^n(x, y, z)$ the extra-stress computed at time t^n . Since (3.21) is a stationary equation, the discretization in time is straightforward:

$$\eta \Delta \mathbf{V}^n + \nabla \cdot \boldsymbol{\Sigma}^n = \nabla P_\infty^n. \quad (3.24)$$

Note that P^n denotes here the pressure that ensures the divergence-free condition at time t^n .

Following [3], we perform a splitting in time on equation (3.23) with two steps. The first step of the splitting includes transport and diffusion (non-local terms). We hence calculate an intermediate value $\Sigma^{n+\frac{1}{2}}$ from the supposed known Σ^n :

$$\frac{\Sigma^{n+1/2} - \Sigma^n}{\delta t} = \mathbf{V}^n \cdot \nabla \Sigma^n + \mathcal{D} \Delta \Sigma^{n+1/2}. \quad (3.25)$$

The second step of the splitting deals with the objective derivative and the source terms (local terms), it consists in solving an ODE in each point of the domain:

$$\frac{\Sigma^{n+1} - \Sigma^{n+\frac{1}{2}}}{\delta t} = f_a(\mathbf{V}^n, \Sigma^{n+\frac{1}{2}}) + 2GD[\mathbf{V}^n] - \frac{1}{\tau} \Sigma^{n+\frac{1}{2}} - \frac{\kappa}{G\tau} \left(\Sigma^{n+\frac{1}{2}} \right)^2. \quad (3.26)$$

As stated before, it remains to compute the pressure P^n that ensures the divergence-free condition (3.22) upon the velocity.

Consider the following problem (Σ being known) :

$$\begin{cases} \eta \Delta \mathbf{V} = \nabla P - \nabla \cdot \Sigma, \\ \nabla \cdot \mathbf{V} = 0. \end{cases} \quad (3.27)$$

Finding the velocity and pressure that satisfy both momentum equation and the divergence-free condition is a well-known problem, and many methods already exist in order to solve it. Among them, the Uzawa algorithm [25] is particularly adapted for solving Stokes flows. Considering a pseudo time step δr , the Uzawa algorithm writes:

$$\begin{cases} \eta \Delta \mathbf{V}^{r+1} - \delta r \nabla (\nabla \cdot \mathbf{V}^{r+1}) = \nabla P^r + \nabla \cdot \Sigma, \\ P^{r+1} = P^r - \delta r \nabla \cdot \mathbf{V}^{r+1}. \end{cases} \quad (3.28)$$

Note that δr has to be chosen small enough to ensure the stability of the system, and big enough to ensure quick convergence. Practically we take δr with the same order of magnitude as η . Once $\|P^{r+1} - P^r\|_\infty \leq \|P^{r+1}\|_\infty 10^{-8}$, we consider that the system (3.28) has reached convergence and we iterate in time.

3.2. Discretization in space

In this section we describe the set of finite difference methods used for the discretization of (3.21)-(3.23) in space. Let us subdivide the domain into the following regular cartesian mesh: $x_i = i \delta x$, $y_j = j \delta y$, $z_k = k \delta z$. The velocity nodes are placed in the following way:

$$\begin{aligned} u_{i,j,k} &= u(x_{i-\frac{1}{2}}, y_j, z_k), \\ v_{i,j,k} &= v(x_i, y_{j-\frac{1}{2}}, z_k), \\ w_{i,j,k} &= w(x_i, y_j, z_{k-\frac{1}{2}}). \end{aligned}$$

The pressure and the extra stress components are given on the nodes of the mesh:

$$\begin{aligned} P_{i,j,k} &= P(x_i, y_j, z_k), \\ \Sigma_{i,j,k} &= \Sigma(x_i, y_j, z_k). \end{aligned}$$

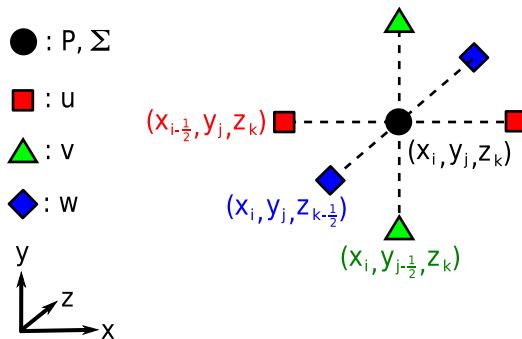


Figure 7: schematic view of a MAC mesh, relative placement of the nodes.

This placement for the variables \mathbf{V} , P and Σ correspond to a staggered grid, as represented on Figure 7. For simplicity, from now on, we leave the subscript n that stands for the discretization in time.

3.2.1. Discretization of the momentum equation

In this section we focus on the space discretization of the equation :

$$\eta \Delta \mathbf{V} - \delta r \nabla (\nabla \cdot \mathbf{V}) - \nabla P + \nabla \cdot \Sigma = 0, \quad (3.29)$$

We use the MAC scheme for the discretization of the first three terms of (3.29). This scheme consists in evaluating the derivative in (3.29) by using centered finite difference. The placement of the variables on a staggered grid as described above ensures the second order convergence of \mathbf{V} by using centered finite differences. In our case, the difficulty lies on the discretization of the term $\nabla \cdot \Sigma$.

The extra stress contribution $\nabla \cdot \Sigma$ in the momentum equation is defined in the following way:

$$\nabla \cdot \Sigma = \begin{pmatrix} \partial_x \Sigma^{xx} + \partial_y \Sigma^{xy} + \partial_z \Sigma^{xz} \\ \partial_x \Sigma^{xy} + \partial_y \Sigma^{yy} + \partial_z \Sigma^{yz} \\ \partial_x \Sigma^{xz} + \partial_y \Sigma^{yz} + \partial_z \Sigma^{zz} \end{pmatrix}.$$

According to the MAC discretization, the first component of $\nabla \cdot \Sigma$ has to be evaluated in a staggered cell centered on $x_{i-\frac{1}{2},j,k}$. The discretization of $\partial_x \Sigma^{xx}$ is straightforward since the Σ nodes are well placed to evaluate the x derivatives at $x_{i-\frac{1}{2},j,k}$:

$$\partial_x \Sigma^{xx}(x_{i-\frac{1}{2}}, y_j, z_k) \sim \frac{\Sigma_{i,j,k}^{xx} - \Sigma_{i-1,j,k}^{xx}}{\delta x}.$$

The other terms $\partial_y \Sigma^{xy}$ and $\partial_z \Sigma^{xz}$ need some interpolation in order to be evaluated properly. As shown below, introducing the values of Σ on eight nodes around the considered point, one can write

$$\begin{aligned} \partial_y \Sigma^{xy}(x_{i-\frac{1}{2}}, y_j, z_k) &\sim \frac{\overline{\Sigma_{i,j,k}^{xy}} - \overline{\Sigma_{i,j-1,k}^{xy}}}{\delta y}, \\ \partial_z \Sigma^{xz}(x_{i-\frac{1}{2}}, y_j, z_k) &\sim \frac{\overline{\Sigma_{i,j,k}^{xz}} - \overline{\Sigma_{i,j,k-1}^{xz}}}{\delta z}, \end{aligned}$$

where the interpolated values are:

$$\begin{aligned} \overline{\Sigma_{i,j,k}^{xy}} &= \frac{1}{4} (\Sigma_{i,j,k}^{xy} + \Sigma_{i-1,j,k}^{xy} + \Sigma_{i,j+1,k}^{xy} + \Sigma_{i-1,j+1,k}^{xy}), \\ \overline{\Sigma_{i,j,k}^{xz}} &= \frac{1}{4} (\Sigma_{i,j,k}^{xz} + \Sigma_{i-1,j,k}^{xz} + \Sigma_{i,j,k+1}^{xz} + \Sigma_{i-1,j,k+1}^{xz}). \end{aligned}$$

Inside the domain we hence have:

$$\begin{aligned} \left(\nabla \cdot \Sigma(x_{i-\frac{1}{2}}, y_j, z_k) \right) \cdot \vec{e}_x &\sim \frac{\Sigma_{i,j,k}^{xx} - \Sigma_{i-1,j,k}^{xx}}{\delta x} \\ &+ \frac{\Sigma_{i,j+1,k}^{xy} + \Sigma_{i-1,j+1,k}^{xy} - \Sigma_{i,j-1,k}^{xy} - \Sigma_{i-1,j-1,k}^{xy}}{4 \delta y} \\ &+ \frac{\Sigma_{i,j,k+1}^{xz} + \Sigma_{i-1,j,k+1}^{xz} - \Sigma_{i,j,k-1}^{xz} - \Sigma_{i-1,j,k-1}^{xz}}{4 \delta z}. \end{aligned}$$

In a similar way, we obtain:

$$\begin{aligned} \left(\nabla \cdot \Sigma(x_i, y_{j-\frac{1}{2}}, z_k) \right) \cdot \vec{e}_y &\sim \frac{\Sigma_{i,j,k}^{yy} - \Sigma_{i,j-1,k}^{yy}}{\delta y} \\ &+ \frac{\Sigma_{i+1,j,k}^{xy} + \Sigma_{i+1,j-1,k}^{xy} - \Sigma_{i-1,j,k}^{xy} - \Sigma_{i-1,j-1,k}^{xy}}{4 \delta x} \\ &+ \frac{\Sigma_{i,j,k+1}^{yz} + \Sigma_{i,j-1,k+1}^{yz} - \Sigma_{i,j,k-1}^{yz} - \Sigma_{i,j-1,k-1}^{yz}}{4 \delta z}, \end{aligned}$$

and

$$\begin{aligned} \left(\nabla \cdot \Sigma(x_i, y_j, z_{k-\frac{1}{2}}) \right) \cdot \vec{e}_z &\sim \frac{\Sigma_{i,j,k}^{zz} - \Sigma_{i,j,k-1}^{zz}}{\delta z} \\ &+ \frac{\Sigma_{i+1,j,k}^{xz} + \Sigma_{i+1,j,k-1}^{xz} - \Sigma_{i-1,j,k}^{xz} - \Sigma_{i-1,j,k-1}^{xz}}{4 \delta x} \\ &+ \frac{\Sigma_{i,j+1,k}^{yz} + \Sigma_{i,j+1,k-1}^{yz} - \Sigma_{i,j-1,k}^{yz} - \Sigma_{i,j-1,k-1}^{yz}}{4 \delta y}. \end{aligned}$$

3.2.2. Discretization of the constitutive equation

We recall that we apply a splitting scheme to the constitutive equation (3.23), to end up with the to substeps (3.25) and (3.26). We consider the first step of the splitting (3.25) for the constitutive equation. The only terms containing space derivatives are the advection term and the diffusion term. The advection term $\mathbf{V} \cdot \nabla \Sigma$ is discretized by using an high order scheme (WENO 5, [15]) in order to limit numerical diffusion. The diffusion term is discretized with the second order 5-points scheme:

$$\begin{aligned} \Delta \Sigma(x_i, y_j, z_k) &\sim \frac{\Sigma_{i+1,j,k} - 2 \Sigma_{i,j,k} + \Sigma_{i-1,j,k}}{\delta x^2} \\ &+ \frac{\Sigma_{i,j+1,k} - 2 \Sigma_{i,j,k} + \Sigma_{i,j-1,k}}{\delta y^2} \\ &+ \frac{\Sigma_{i,j,k+1} - 2 \Sigma_{i,j,k} + \Sigma_{i,j,k-1}}{\delta z^2}. \end{aligned}$$

In the second step of the splitting (3.25), the only terms containing space derivatives are \mathbf{D} and $\mathbf{\Omega}$. These terms need to be approached at the Σ nodes (x_i, y_j, z_k) . They read:

$$\mathbf{D} = \frac{\nabla \mathbf{V} + \nabla \mathbf{V}^t}{2},$$

$$\mathbf{\Omega} = \frac{\nabla \mathbf{V} - \nabla \mathbf{V}^t}{2}.$$

We hence need to approach:

$$\nabla \mathbf{V} = \begin{pmatrix} \partial_x u & \partial_y u & \partial_z u \\ \partial_x v & \partial_y v & \partial_z v \\ \partial_x w & \partial_y w & \partial_z w \end{pmatrix}.$$

The discretization of the diagonal components $\partial_x u$, $\partial_y v$ and $\partial_z w$ is straightforward since u , v and w are placed on the grid such that the divergence can be evaluated at the second order at the Σ nodes (x_i, y_j, z_k) . Hence,

$$\partial_x u(x_i, y_j, z_k) \sim \frac{u_{i+1,j,k} - u_{i,j,k}}{\delta x},$$

$$\partial_y v(x_i, y_j, z_k) \sim \frac{v_{i,j+1,k} - v_{i,j,k}}{\delta y},$$

$$\partial_z w(x_i, y_j, z_k) \sim \frac{w_{i,j,k+1} - w_{i,j,k}}{\delta z}.$$

Following Section 3.2.1, the extra-diagonal components of $\nabla \mathbf{V}$ need some interpolations to be evaluated properly, for instance:

$$\partial_y u(x_i, y_j, z_k) \sim \frac{\overline{u_{i,j,k}} - \overline{u_{i,j-1,k}}}{\delta y},$$

where

$$\overline{u_{i,j,k}} = \frac{1}{4} (u_{i,j,k} + u_{i-1,j,k} + u_{i,j+1,k} + u_{i-1,j+1,k}),$$

which gives

$$\partial_y u(x_i, y_j, z_k) \sim \frac{u_{i,j+1,k} + u_{i-1,j+1,k} - u_{i,j-1,k} - u_{i-1,j-1,k}}{4 \delta y}.$$

In the same way, we get:

$$\begin{aligned}\partial_z u(x_i, y_j, z_k) &\sim \frac{u_{i,j,k+1} + u_{i-1,j,k+1} - u_{i,j,k-1} - u_{i-1,j,k-1}}{4 \delta z}, \\ \partial_x v(x_i, y_j, z_k) &\sim \frac{v_{i+1,j,k} + v_{i+1,j-1,k} - v_{i-1,j,k} - v_{i-1,j-1,k}}{4 \delta x}, \\ \partial_z v(x_i, y_j, z_k) &\sim \frac{v_{i,j,k+1} + v_{i,j-1,k+1} - v_{i,j,k-1} - v_{i,j-1,k-1}}{4 \delta z}, \\ \partial_x w(x_i, y_j, z_k) &\sim \frac{w_{i+1,j,k} + w_{i+1,j,k-1} - w_{i-1,j,k} - w_{i-1,j,k-1}}{4 \delta x}, \\ \partial_y w(x_i, y_j, z_k) &\sim \frac{w_{i,j+1,k} + w_{i,j+1,k-1} - w_{i,j-1,k} - w_{i,j-1,k-1}}{4 \delta y}.\end{aligned}$$

3.3. Taking into account the boundary conditions on the T-shaped geometry

In this paper, we prescribe a particular geometry which is the shape of our micro-fluidic junction. As mentioned above, for the sake of simplicity we discretize the equations on a cartesian grid. In order to take into account the boundary conditions in the case of junction geometries, a fictitious domain method is used. The purpose of fictitious domain methods, first introduced in [21], is to approximate the solutions of partial differential equations posed on a complex domain by using a non-conformal mesh (in our case cartesian). In the following, we use the L^2 penalty method presented in [2], [23].

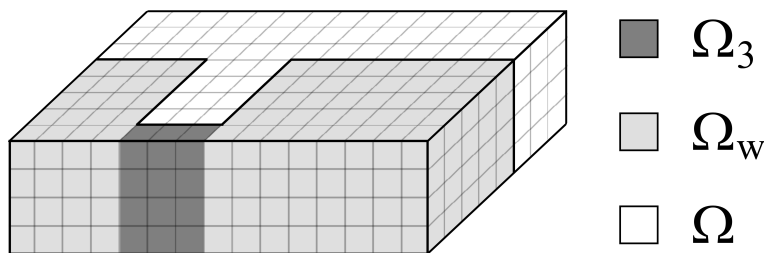


Figure 8: Schematic view of the three computational domains involved in the fictitious domain method used in this paper.

In Sections 3.3.1 and 3.3.2, we discriminate three computational domains (depicted in Figure 8): the "physical" domain Ω , the "inlet" domain Ω_3 and the "wall" domain Ω_w . We also denote Γ_t (r.p. $\Gamma_{d,f,b,l,r}$) the top (r.p. down, front, back, left, right) boundary of the computational domain, and $\Omega_c = \Omega \cup \Omega_w \cup \Omega_3$ the computational domain itself.

3.3.1. Momentum equation

Recall the momentum equation and its boundary conditions:

$$\eta \Delta \mathbf{V} + \nabla \cdot \boldsymbol{\Sigma} = \nabla P \quad \text{in } \Omega, \quad (3.30)$$

$$\nabla \cdot \mathbf{V} = 0,$$

$$\mathbf{V} = 0 \quad \text{on } \Gamma_w, \quad (3.31)$$

$$\mathbf{V} = \mathbf{V}^{\delta P} \quad \text{on } \Gamma_3, \quad (3.32)$$

$$\mathbf{V} = \mathbf{V}^{\delta P_{1,2}}, \quad \underline{\text{or}} \quad \partial_{\bar{n}} \mathbf{V} = 0 \quad \text{on } \Gamma_{1,2}. \quad (3.33)$$

Since the borders $\Gamma_{1,2}$ match the computational boundaries $\Gamma_{l,r}$, the conditions (3.33) are set in a standard way. The others boundary conditions (3.31)-(3.32) are imposed through a penalty term. The modified system to be solved on the rectangular computational domain writes:

$$\eta \Delta \mathbf{V} + \nabla \cdot \boldsymbol{\Sigma} - \frac{1}{\varepsilon} (\mathbf{1}_{\Omega_w} \mathbf{V} + \mathbf{1}_{\Omega_3} (\mathbf{V} - \mathbf{V}^{\delta P})) = \nabla P \quad \text{in } \Omega_c, \quad (3.34)$$

$$\nabla \cdot \mathbf{V} = 0,$$

$$\mathbf{V} = 0 \quad \text{on } \Gamma_{t,d,b}, \quad (3.35)$$

$$\mathbf{V} = \mathbf{1}_{\Gamma_3} \mathbf{V}^{\delta P} \quad \text{on } \Gamma_f, \quad (3.36)$$

$$\mathbf{V} = \mathbf{1}_{\Gamma_{1,2}} \mathbf{V}^{\delta P_{1,2}}, \quad \underline{\text{or}} \quad \partial_{\bar{n}} \mathbf{V} = 0 \quad \text{on } \Gamma_{l,r}, \quad (3.37)$$

where $0 < \varepsilon \ll 1$ and $\mathbf{1}_B$ is the characteristic function of the domain B (*i.e.* $\mathbf{1}_B(x, y, z) = 1$ if $(x, y, z) \in B$ and $\mathbf{1}_B(x, y, z) = 0$ elsewhere). It is possible to show that, as $\varepsilon \rightarrow 0$ the solution of the problem (3.34)- (3.37), restricted to Ω converges to the solution of (3.30)- (3.31) in $H^1(\Omega)$ (we refer to [2] [4] for theoretical work on the subject).

3.3.2. Constitutive equation

Let us recall the first step of the time scheme on the constitutive equation, with the associated boundary conditions :

$$(Id - \delta t \Delta) \boldsymbol{\Sigma}^{n+1/2} = \boldsymbol{\Sigma}^n - \delta t \mathbf{V}^n \cdot \nabla \boldsymbol{\Sigma}^n \quad \text{in } \Omega, \quad (3.38)$$

$$\partial_{\bar{n}} \boldsymbol{\Sigma}^{n+1/2} = 0 \quad \text{on } \Gamma_w. \quad (3.39)$$

$$\boldsymbol{\Sigma}^{n+1/2} = \boldsymbol{\Sigma}^{\delta P} \quad \text{on } \Gamma_3, \quad (3.40)$$

$$\boldsymbol{\Sigma}^{n+1/2} = \boldsymbol{\Sigma}^{\delta P_{1,2}}, \quad \underline{\text{or}} \quad \partial_{\bar{n}} \boldsymbol{\Sigma}^{n+1/2} = 0 \quad \text{on } \Gamma_{1,2}, \quad (3.41)$$

As above, the boundary conditions (3.41) on $\Gamma_{1,2}$ are set in a standard way. The Neumann condition (3.39) and the Dirichlet condition (3.40) are imposed through the penalty method :

$$\begin{aligned} & \mathbf{1}_{\Omega \cup \Omega_3} \Sigma^{n+1/2} - \delta t \nabla \cdot ((\mathbf{1}_{\Omega \cup \Omega_3} + \varepsilon \mathbf{1}_{\Omega_w}) \nabla \Sigma^{n+1/2}) \\ & + \frac{1}{\varepsilon} \mathbf{1}_{\Omega_3} (\Sigma^{n+1/2} - \Sigma^{\delta P}) = \mathbf{1}_{\Omega \cup \Omega_3} (\Sigma^n - \delta t \mathbf{V}^n \cdot \nabla \Sigma^n) \quad \text{in } \Omega, \end{aligned} \quad (3.42)$$

$$\Sigma^{n+1/2} = \mathbf{1}_{\Gamma_3} \Sigma^{\delta P} \quad \text{on } \Gamma_f, \quad (3.43)$$

$$\partial_{\vec{n}} \Sigma^{n+1/2} = 0 \quad \text{on } \Gamma_{t,d,b}, \quad (3.44)$$

$$\Sigma^{n+1/2} = \mathbf{1}_{\Gamma_{1,2}} \Sigma^{\delta P_{1,2}}, \quad \text{or} \quad \partial_{\vec{n}} \Sigma^{n+1/2} = 0 \quad \text{on } \Gamma_{l,r}, \quad (3.45)$$

Again, we refer the reader to [2] [4] for proofs of convergence between (3.38)-(3.41) and (3.42)- (3.45) as $\varepsilon \rightarrow 0$.

As many fictitious domain methods, the penalty method usually induce a loss of accuracy of the numerical scheme. In our case, there is no loss of accuracy, due to the fact that the mesh is actually conformal to the geometry of the channel (see Figure 8).

3.4. Stability issues

The numerical scheme in time introduced in Section 3.1 presents an explicit coupling between the momentum equation (3.21) and the constitutive equation (3.23). In this section we highlight the fact that this explicit coupling may induce numerical instabilities that disappear if the time step is chosen small enough. For the sake of simplicity, we study a linear 2D version of the model (3.21)-(3.23) in its dimensionless form:

$$\alpha \Delta \mathbf{V} + \nabla \cdot \Sigma = \nabla P + \mathbf{F}, \quad (3.46)$$

$$\nabla \cdot \mathbf{V} = 0, \quad (3.47)$$

$$\partial_t \Sigma = \frac{(\nabla \mathbf{V})^t + \nabla \mathbf{V}}{2} - \Sigma. \quad (3.48)$$

For the sake of simplicity the domain is $\Omega =]0, 2\pi[\times]0, 2\pi[$ and we consider solutions that are periodic in both directions (x, y) . The external force \mathbf{F} ensures a non-zero solution. We first show that, if Σ is a solution of (3.46)-(3.48), then it grows at most linearly.

Proposition 1. *Let (\mathbf{V}, Σ) be a bi-periodic (in space) solution of (3.46)-(3.48) associated with the initial condition Σ_0 , then there exists $c > 0$ such that :*

$$\|\Sigma\|_{L^2} \leq \|\Sigma_0\|_{L^2} + ct. \quad (3.49)$$

Proof. For any periodic function f we denote by $\hat{f}_{k,l}$ the Fourier mode defined by:

$$\hat{f}_{k,l} = \iint_{\Omega} f(x, y) e^{-\mathcal{I}(kx+ly)} dx dy, \quad (3.50)$$

where \mathcal{I} is the imaginary unit (for the sake of simplicity we drop the indexes k, l from now on). By performing the above Fourier transform on (3.46)-(3.47), we obtain:

$$-\alpha(k^2 + l^2) \hat{u} + \mathcal{I} k \hat{\Sigma}^{xx} + \mathcal{I} l \hat{\Sigma}^{xy} = \mathcal{I} k \hat{P} + \hat{F}^x, \quad (3.51)$$

$$-\alpha(k^2 + l^2) \hat{v} + \mathcal{I} k \hat{\Sigma}^{xy} + \mathcal{I} l \hat{\Sigma}^{yy} = \mathcal{I} l \hat{P} + \hat{F}^y, \quad (3.52)$$

$$k \hat{u} + l \hat{v} = 0. \quad (3.53)$$

Some elementary algebraic operations lead to the expression of \hat{u} and \hat{v} as a function of $\hat{\Sigma}$:

$$\begin{aligned} \hat{u} &= \frac{1}{\alpha(k^2 + l^2)^2} \left(\mathcal{I} k l^2 (\hat{\Sigma}^{xx} - \hat{\Sigma}^{yy}) + \mathcal{I} l (l^2 - k^2) \hat{\Sigma}^{xy} - l^2 \hat{F}^x + k l \hat{F}^y \right), \\ \hat{v} &= \frac{1}{\alpha(k^2 + l^2)^2} \left(\mathcal{I} k^2 l (\hat{\Sigma}^{yy} - \hat{\Sigma}^{xx}) + \mathcal{I} k (k^2 - l^2) \hat{\Sigma}^{xy} - k^2 \hat{F}^y + k l \hat{F}^x \right). \end{aligned}$$

Applying the same procedure on Equation (3.48) we get:

$$\partial_t \hat{\Sigma} = -\hat{\Sigma} + \frac{\mathcal{I}}{2} \begin{pmatrix} 2k \hat{u} \\ k \hat{v} + l \hat{u} \\ 2l \hat{v} \end{pmatrix}. \quad (3.54)$$

Knowing \hat{u} and \hat{v} we obtain:

$$\partial_t \hat{\Sigma} = -A \hat{\Sigma} + B, \quad (3.55)$$

where B depends only on \hat{F}^x and \hat{F}^y . The matrix A writes:

$$A = \frac{1}{c} \begin{pmatrix} a & b & -a \\ b & \frac{b^2}{a} & -b \\ -a & -b & a \end{pmatrix} + Id, \quad (3.56)$$

where:

$$a = k^2 l^2, \quad (3.57)$$

$$b = k l (l^2 - k^2), \quad (3.58)$$

$$c = (k^2 + l^2)^2. \quad (3.59)$$

The matrix A is symmetric positive definite since, $\forall X = (x, y, z)^t \neq 0$:

$$\begin{aligned} X^t A X &= \frac{1}{\alpha c} \left(a x^2 + \frac{b^2}{a} y^2 + a z^2 + 2 b x y - 2 a x z - 2 b y z \right) + x^2 + y^2 + z^2, \\ &= \left(\sqrt{a} x + \frac{b}{\sqrt{a}} y - \sqrt{a} z \right)^2 + x^2 + y^2 + z^2 > 0. \end{aligned}$$

The term $-A\hat{\Sigma}$ in (3.55) is hence an exponential decay term. The term B in (3.55) being constant, we expect the growth of $|\hat{\Sigma}|$ to be at most linear in time, as for $\|\hat{\Sigma}\|_{l^2}$ and hence $\|\Sigma\|_{L^2}$ (through Parseval's theorem). \square

In the following paragraph, we show that this property is conserved in the numerical scheme introduced in Sections 3.1 and 3.1, provided that the time step is small enough.

For more simplicity we suppose the discretization steps in space δx and δy to be the same (denoted h). Let us recall the numerical scheme introduced in Sections 3.1 and 3.1, in the particular case of the model (3.46)-(3.47) (the pressure is supposed to be known):

$$\begin{aligned} &\frac{1}{h}(u_{i+1,j}^n + u_{i-1,j}^n + u_{i,j+1}^n + u_{i,j-1}^n - 4u_{i,j}^n) + (\Sigma^{xx})_{i,j}^n - (\Sigma^{xx})_{i,j}^n \\ &\quad + \frac{1}{4} [(\Sigma^{xy})_{i,j+1}^n + (\Sigma^{xy})_{i-1,j+1}^n - (\Sigma^{xy})_{i,j-1}^n - (\Sigma^{xy})_{i-1,j-1}^n] \quad (3.60) \\ &\quad = P_{i,j} - P_{i-1,j} + h F_{i,j}^x, \end{aligned}$$

$$\begin{aligned} &\frac{1}{h}(v_{i+1,j}^n + v_{i-1,j}^n + v_{i,j+1}^n + v_{i,j-1}^n - 4v_{i,j}^n) + (\Sigma^{yy})_{i,j}^n - (\Sigma^{yy})_{i,j}^n \\ &\quad + \frac{1}{4} [(\Sigma^{xy})_{i+1,j}^n + (\Sigma^{xy})_{i+1,j-1}^n - (\Sigma^{xy})_{i-1,j}^n - (\Sigma^{xy})_{i-1,j-1}^n] \quad (3.61) \\ &\quad = P_{i,j} - P_{i,j-1} + h F_{i,j}^y, \end{aligned}$$

$$u_{i+1,j}^n - u_{i,j}^n + v_{i,j+1}^n - v_{i,j}^n = 0, \quad (3.62)$$

$$\Sigma_{i,j}^{n+1} = \Sigma_{i,j}^n - \delta t \Sigma_{i,j}^n + \delta t D_{i,j}^n. \quad (3.63)$$

Proposition 2. *Assume that :*

$$\delta t < \frac{32\alpha}{1 + 16\alpha}, \quad (3.64)$$

then the numerical scheme (3.60) (3.63) is stable, i.e there exists $c > 0$ such that:

$$\|\Sigma^n\|_{l^2} \leq \|\Sigma^0\|_{l^2} + c n \delta t. \quad (3.65)$$

Proof. We introduce the following Fourier transform for any discrete periodic field $f_{i,j}$

$$\hat{f}_{k,l} = \sum_{i=0}^{N-1} \sum_{j=0}^{N-1} f_{i,j} e^{-\mathcal{I}h(ik+jl)}. \quad (3.66)$$

Let

$$\xi^- = 1 - e^{-\mathcal{I}kh}, \quad \xi^+ = e^{\mathcal{I}kh} - 1, \quad (3.67)$$

$$\eta^- = 1 - e^{-\mathcal{I}lh}, \quad \eta^+ = e^{\mathcal{I}lh} - 1. \quad (3.68)$$

We have :

$$\xi^+ - \xi^- = \xi^+\xi^-, \quad \xi^+(2 - \xi^-) = \xi^+ + \xi^-, \quad (3.69)$$

$$\eta^+ - \eta^- = \eta^+\eta^-, \quad \eta^+(2 - \eta^-) = \eta^+ + \eta^-. \quad (3.70)$$

The calculation can be performed as in the continuous case. By applying the Fourier transform (3.66) to the numerical scheme (3.60)-(3.62), we get:

$$\begin{aligned} \frac{\alpha}{h}(\xi^+\xi^- + \eta^+\eta^-) \hat{u}^n + \xi^-(\hat{\Sigma}^{xx})^n + \frac{1}{4}(\eta^+ + \eta^-)(2 - \xi^-)(\hat{\Sigma}^{xy})^n &= \xi^- \hat{P} + h \hat{F}^x, \\ \frac{\alpha}{h}(\xi^+\xi^- + \eta^+\eta^-) \hat{v}^n + \eta^-(\hat{\Sigma}^{yy})^n + \frac{1}{4}(\xi^+ + \xi^-)(2 - \eta^-)(\hat{\Sigma}^{xy})^n &= \eta^- \hat{P} + h \hat{F}^y, \\ \xi^+ \hat{u}^n + \eta^+ \hat{v}^n &= 0. \end{aligned}$$

We obtain \hat{P} as in the continuous case :

$$\hat{P} = \frac{\xi^+\xi^-(\hat{\Sigma}^{xx})^n + \eta^+\eta^-(\hat{\Sigma}^{yy})^n + \frac{1}{2}(\xi^+ + \xi^-)(\eta^+ + \eta^-)(\hat{\Sigma}^{xy})^n - h(\xi^+ \hat{F}^x + \eta^+ \hat{F}^y)}{\xi^+\xi^- + \eta^+\eta^-}. \quad (3.71)$$

Therefore, \hat{u} and \hat{v} can be evaluated in terms of $\hat{\Sigma}$ and \hat{F} :

$$\begin{aligned} \hat{u}^n &= \frac{h}{\alpha(\xi^+\xi^- + \eta^+\eta^-)^2} \left[\xi^- \eta^+ \eta^- ((\hat{\Sigma}^{yy})^n - (\hat{\Sigma}^{xx})^n) \right. \\ &\quad \left. + \frac{(\xi^+\xi^- - \eta^+\eta^-)(\xi^+ + \xi^-)(\eta^+ + \eta^-)}{4\xi^+} (\hat{\Sigma}^{xy})^n \right] + f(\hat{F}^x, \hat{F}^y), \quad (3.72) \end{aligned}$$

$$\begin{aligned} \hat{v}^n &= \frac{h}{\alpha(\xi^+\xi^- + \eta^+\eta^-)^2} \left[\eta^- \xi^+ \xi^- ((\hat{\Sigma}^{xx})^n - (\hat{\Sigma}^{yy})^n) \right. \\ &\quad \left. + \frac{(\eta^+\eta^- - \xi^+\xi^-)(\xi^+ + \xi^-)(\eta^+ + \eta^-)}{4\eta^+} (\hat{\Sigma}^{xy})^n \right] + g(\hat{F}^x, \hat{F}^y), \quad (3.73) \end{aligned}$$

where f and g are terms that depend only on \hat{F} (not developed here).

Following Sections 3.1 and 3.2, the discretization of the evolution equation (3.48) reads:

$$\Sigma_{i,j}^{n+1} = \Sigma_{i,j}^n - \delta t \Sigma_{i,j}^n + \delta t D_{i,j}^n, \quad (3.74)$$

where $D_{i,j}^n$ is given by

$$D_{i,j}^n = \frac{1}{h} \begin{pmatrix} u_{i+1,j}^n - u_{i,j}^n \\ \frac{1}{4}(u_{i+1,j+1}^n - u_{i+1,j-1}^n + u_{i,j+1}^n - u_{i,j-1}^n \\ + v_{i+1,j+1}^n - v_{i-1,j+1}^n + v_{i+1,j}^n - v_{i-1,j}^n) \\ v_{i,j+1}^n - v_{i,j}^n \end{pmatrix}. \quad (3.75)$$

We then apply the discrete Fourier transform on the discretized evolution equation (3.77) to obtain:

$$\hat{\Sigma}_{i,j}^{n+1} = \hat{\Sigma}_{i,j}^n - \delta t \hat{\Sigma}_{i,j}^n + \frac{\delta t}{h} \begin{pmatrix} \xi^+ \hat{u}^n \\ \frac{1}{4} [(\eta^+ + \eta^-)(\xi^+ + 1) \hat{u}^n + (\xi^+ + \xi^-)(\eta^+ + 1) \hat{v}^n] \\ \eta^+ \hat{v}^n \end{pmatrix}. \quad (3.76)$$

Recalling that \hat{u}^n and \hat{v}^n depends on $\hat{\Sigma}^n$ (see Equations (3.72) and (3.73)), then (3.76) can be rewritten under the form

$$\hat{\Sigma}_{i,j}^{n+1} = \hat{\Sigma}_{i,j}^n - \delta t A \hat{\Sigma}_{i,j}^n + B, \quad (3.77)$$

where B is a constant term depending only on \hat{F} , and the matrix A writes

$$A = \frac{1}{\alpha c} \begin{pmatrix} a & b & -a \\ b & \frac{b^2}{a} & -b \\ -a & -b & a \end{pmatrix} + Id, \quad (3.78)$$

with

$$\begin{aligned} a &= \xi^+ \xi^- \eta^+ \eta^- = 4(\cos(kh) + 1)(\cos(lh) + 1), \\ b &= \frac{1}{4}(\eta^+ \eta^- - \xi^+ \xi^-)(\xi^+ + \xi^-)(\eta^+ + \eta^-) \\ &= (\cos(kh) - \cos(lh)) \sin(kh) \sin(lh), \\ c &= (\xi^+ \xi^- + \eta^+ \eta^-)^2 = 4(\cos(kh) + \cos(lh) + 2)^2. \end{aligned}$$

The matrix A has exactly the same structure as the one used in the proof of Proposition 1. Hence A is symmetric positive definite. Moreover, simple linear combinations show that the eigenvectors of A are :

$$\begin{pmatrix} 1 \\ 0 \\ 1 \end{pmatrix}, \quad \begin{pmatrix} b \\ -a \\ 0 \end{pmatrix}, \quad \begin{pmatrix} a \\ b \\ -a \end{pmatrix},$$

associated respectively with the eigenvalues

$$1, \quad 1, \quad \frac{b^2}{\alpha a c} + 1.$$

In order to deal with linear growth of $|\hat{\Sigma}|$ in the numerical scheme (3.77), the time step δt has to be small enough to ensure stability. Typically, this condition reads

$$\delta t < \frac{2}{\rho(A)}, \quad (3.79)$$

where $\rho(A)$ is the spectral radius of A . Since $a > 0$ and $c > 0$, we have:

$$\rho(A) = \frac{b^2}{\alpha a c} + 1. \quad (3.80)$$

Moreover, one can compute

$$\begin{aligned} \frac{b^2}{a c} &\leq \frac{(\cos(kh) - \cos(lh))^2 \sin^2(kh) \sin^2(lh)}{16(\cos(kh) + 1)(\cos(lh) + 1)(\cos(kh) + \cos(lh) + 2)^2} \\ &= \frac{(\cos(kh) - \cos(lh))^2 (1 - \cos(kh))(1 - \cos(lh))}{16(\cos(kh) + \cos(lh) + 2)^2} \\ &\leq \frac{(1 - \cos(kh))(1 - \cos(lh))}{4(\cos(kh) + \cos(lh) + 2)^2} \\ &\leq \frac{1}{16}, \end{aligned}$$

which furnishes

$$\rho(A) \leq \frac{1}{16\alpha} + 1. \quad (3.81)$$

Then a sufficient condition for stability reads

$$\delta t < \frac{32\alpha}{1 + 16\alpha}. \quad (3.82)$$

□

Condition (3.82) may not be too restrictive since the values of α are never too small in our simulations. Indeed, the CFL condition for the transport part of the full model (2.12) is usually more restrictive than the condition (3.82). The above calculation shows that the numerical scheme described in Sections 3.1 and 3.2 is not appropriate for models such as the upper convected Maxwell model, for which α has to be taken small (as a regularization parameter).

4. Numerical Results

In the following section we present the different numerical results obtained on the model (2.12) with the numerical method described in Section 3. We focused on the following rheological parameters:

$$\begin{aligned}\eta &= 1 \text{ Pa}\cdot\text{s} , \\ G &= 150 \text{ Pa} , \\ \tau &= 0.5 \text{ s} , \\ a &= 0.9 , \\ \kappa &= 0.3 .\end{aligned}$$

Such a choice of parameters ensures the non-monotonicity of the flow curve $T_{xz}(\dot{\gamma})$ as well as a reasonable growth of the extensional viscosity $\eta_e(\dot{\epsilon}) = \frac{\Sigma_{xx}}{\dot{\epsilon}}$. In what follows, the cross sections of the channels are squares of size $1 \text{ mm} \times 1 \text{ mm}$ and we let vary the other characteristic lengths of the junction (L_1 , L_2 and L_3). The spatial steps are chosen as follows:

$$\delta x = \delta y = \delta z = 2 \cdot 10^{-4} \text{ m} ,$$

which corresponds to a resolution of 50×50 for the cross-section.

4.1. Choice of the model

In this section, the choice of the non-linear model given in Section 2.1.2 is discussed. In Section 2.1.1 we claimed that the linear model exhibits some non-physical behavior in the case of a constant extensional strain. From now on, instead of studying a one way coupling (constant given strain $\dot{\epsilon}$) as in Section 2.1.1, we let the whole system (2.12) evolves in a two-way coupling between the momentum equation and the constitutive equation upon Σ .

4.1.1. A strong extensional case

Let us consider the particular case of a geometry that should induce a strong extensional strain: a six-branched cross junction in which the fluid is injected through four boundaries and exits through two boundaries (see Figure 9). The inlet and outlet boundary conditions used here are the Dirichlet boundary conditions described in Section 2.2. By using the Poiseuille-like model we compute the inlet and outlet velocity and extra-stress profile.

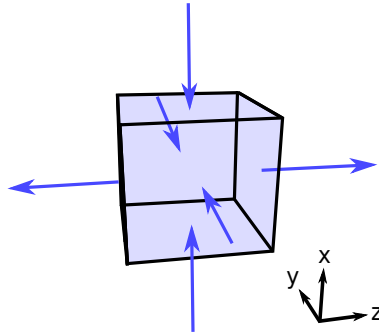


Figure 9: Schematic view of the 6-ways cross-slot domain.

The main interest of such a test case is that it presents a stopping point ($\mathbf{V} = 0$) exactly in the middle of the junction. At this point the strain should be a pure extensional strain. In all what follows we refer to the case $\kappa = 0$ as being the "linear model" while $\kappa = 0.3$ is called the "non-linear" one. We would like to emphasize that even in the case $\kappa = 0$ the complete system is still non-linear. In the same way as in Section 2.1.2 we compare the results given by the linear model ($\kappa = 0$) and the non-linear model ($\kappa = 0.3$).

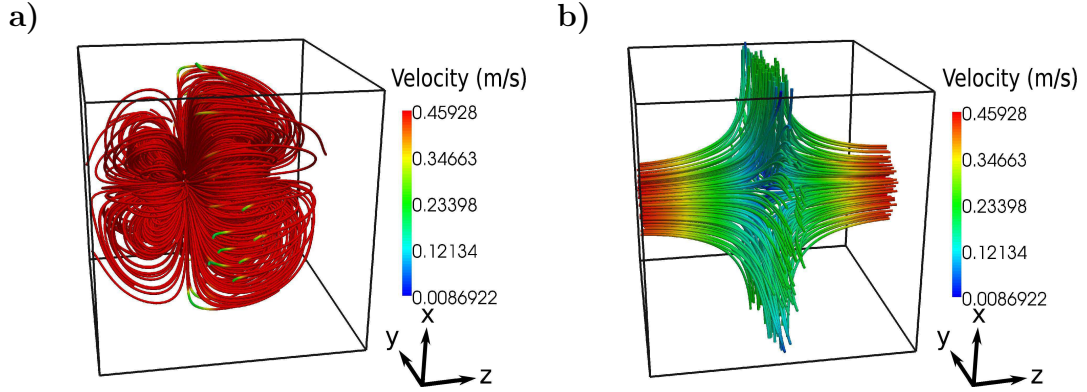


Figure 10: Streamlines resulting from numerical simulations on the model (2.12) in the particular case depicted in Figure 9. Both snapshots are taken at the same time, when some instability is observed on the linear model. On **a)**: the linear model. On **b)**: the non-linear model.

By starting up with the same initial condition $\Sigma = 0$ for both models, we let the system evolve until some instability is observed. As seen on Figure 10, after some time, the two models behave in a different way: the non-linear model (Figure 10**b**) exhibits a stable steady state, whereas, for the non-linear model (Figure 10**a**), the stress grows constantly, leading to a non-physical behavior (energy created from the constitutive equation). As a consequence, it seems necessary to use the non-linear model in this case.

As stated before, the symmetry in this case allows a stopping point where the extra-stress accumulates in the linear case. In the case of an asymmetric T-junction, the situation is a bit more complex and the position of the stop point is less trivial. In the next section, we perform the same tests in the case of an asymmetric junction.

4.1.2. The asymmetric T-shaped junction

In this section we consider the geometry presented in Figure 11. Following Section 4.1.1 our aim is to compare the behaviors of the linear ($\kappa = 0$) and the non-linear ($\kappa = 0.3$) model. The characteristic lengths of the junction are $L_1 = 1 \text{ mm}$, $L_2 = 2 \text{ mm}$, $L_3 = 1 \text{ mm}$.

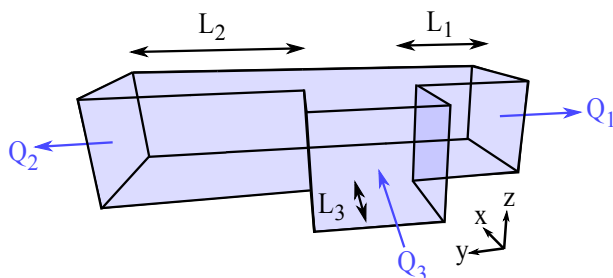


Figure 11: Schematic view of the geometry of a T-shaped junction.

On Figure 12, we observe that after some evolution, the linear model breaks down, as predicted in Section 4.1.1. This result illustrates the necessity to use a non-linear model in order to have a realistic description of the extensional flows we wish to study. Now that we are confident in the validity of our model, so we focus on the case of interest.

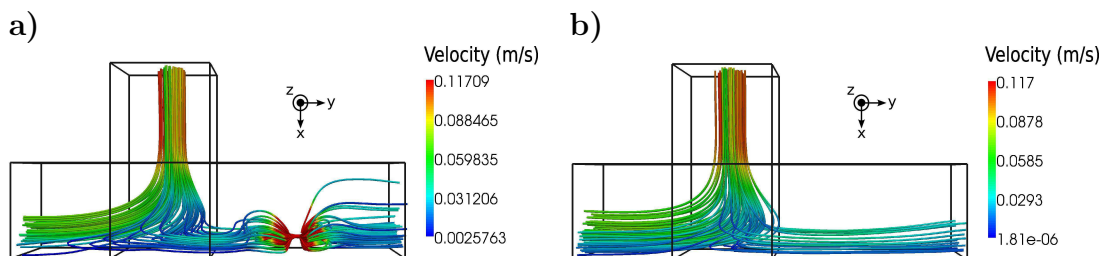


Figure 12: Streamlines resulting from numerical simulations on the model (2.12) in the particular case depicted in Figure 11. Both snapshots are taken at the same time, when some instability is observed on the linear model. On a): the linear model. On b): the non-linear model.

4.2. Flows in an strongly asymmetrical junction : $\frac{L_2}{L_1} = 2$

Results concerning the flow of wormlike micelles in a strongly asymmetrical micro-fluidic junction are presented in this section. First, we attempt to explain the jamming phenomenon depicted in Section 1 by using arguments that involve mainly the so-called "spurt effect" (*i.e.* sudden rise in the flow rate through a pipe above a critical pressure drop) which is only related to the behavior of the fluid under a shear strain. Tridimensional numerical sim-

ulations on the full model (2.12) show that the reduced model approach is not entirely satisfactory.

In what follows, we denote by Q_i the flow rates and δP_i the pressure drops through the boundaries Γ_i where $i = 1, 2, 3$. The flow rate is defined by:

$$Q_i = \int_{\Gamma_i} \mathbf{V} \cdot \vec{n} \, d\Gamma_i. \quad (4.83)$$

Q_3 and δP_3 (inlet) are the input data, whereas (Q_1, Q_2) and $(\delta P_1, \delta P_2)$ (outlets) are the outputs of the model.

4.2.1. Predictions through reduced model approach

In a first attempt to predict the outlet flow rates (Q_1, Q_2) for a given inlet Q_3 , we chose to consider the junction as a simple hydraulic network. In such a network, the pressure can be considered linear for each branch:

$$\delta P_1 = \frac{P_1 - P_0}{L_1}, \quad (4.84)$$

$$\delta P_2 = \frac{P_2 - P_0}{L_2}, \quad (4.85)$$

where P_1 (r.p. P_2) represents the pressure at the outlet Γ_1 (resp. Γ_2). These pressures are supposed to be the same ($P_1 = P_2 = 0$), since we consider outlets at the atmospheric pressure. The pressure P_0 represents an intermediate pressure, which has to be determined.

The flow rates Q_1 , Q_2 and Q_3 must satisfy the following incompressibility condition: $Q_3 = Q_1 + Q_2$. In order to close this model, a relation between the pressure drop and the flow rate must be given.

Usually, a flow rate Q can be linked with a pressure drop δP through a linear relation that can be derived from the Darcy's law. While this law holds in the newtonian case, it is inappropriate for the study of shear-banding fluids such as the Johnson-Segalman's fluid. The Poiseuille-like model 2.16 introduced in Section 2.1.3 allows us to compute the velocity profile of a Johnson-Segalman's fluid through a given section (see Figure 13a) and for a given pressure drop. The equation (4.83) gives us the corresponding flow rate. The Figure 13b presents the relation between Q and δP . We notice that, above a certain value of δP , a sudden augmentation in the flow rate occurs.

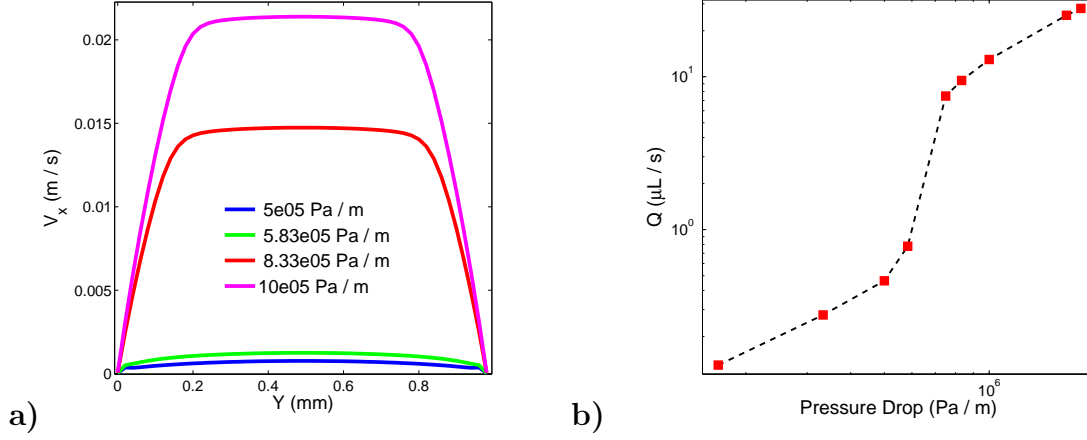


Figure 13: Application of the Poiseuille-like model (2.16). On **a)**: Cut of the velocity profile in the middle of the section, computed for various values of δP . On **b)**: Non-linear relation $Q(\delta P)$ obtained for our fluid.

As mentioned above, the aim is to find the intermediate pressure P_0 such that $Q_3 = Q_1 + Q_2$. For that purpose, we introduce the following iterative algorithm:

0. Initialize P_0^0
1. P^n is known ,
2. Get the pressure drops $\delta P_1^n, \delta P_2^n$, from (4.84)-(4.85),
3. Get the flow rates Q_1^n, Q_2^n , from the relation $Q(\delta P)$ established previously (Figure 13),
4. Update P_0 with: $P_0^{n+1} = P^n + \delta r \frac{Q_3^n - (Q_1^n + Q_2^n)}{\max(Q_1^n, Q_2^n + Q_3^n)}$,
5. Go to 1.

The step δr is taken small enough to ensure stability. We perform the above algorithm for various values of Q_3 , and show the results in Figure 15.

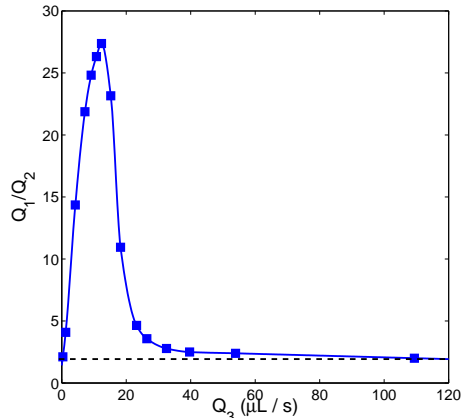


Figure 14: Ratio between the outlet flow rates Q_1/Q_2 as a function of the inlet flow rate Q_3 after convergence of the algorithm described above. Dashed line : theoretical result of a Newtonian fluid.

The Figure 15 shows that for some values of the inlet flow rate Q_3 , the ratio Q_1/Q_2 can rise up to 30 (*i.e.* 30 as much fluid exits through Γ_1 as through Γ_2). This phenomenon is strongly related to the "spurt effect" shown in Figure 13. This study explains partly the jamming observed in the experiments of flows in micro-fluidic T-shaped junctions.

Let us investigate the validity of the reduced model approach. In this matter, we perform a 3D numerical simulation upon the (2.12). For these simulations, the outlet flow rates (Q_1, Q_2) are set as predicted through the above approach for a given value of the inlet flow rate $Q_3 = 56.4 \mu\text{L.s}^{-1}$.

From Figure 15 we notice that the pressure is not the same at each outlet boundary Γ_1 and Γ_2 as it is supposed in the construction of the reduced model. This contradiction might be related to the fact that the redistribution of the flow at the center of the junction is more complex here than in the newtonian case.

The method described in this section doesn't take into account the non-trivial physical process that appears in a flow of wormlike micelles through a junction. It is hence necessary to perform 3D numerical simulations upon the full model (2.12) with the free flow outlet conditions (2.17)-(2.18) in order to be predictive in this case.

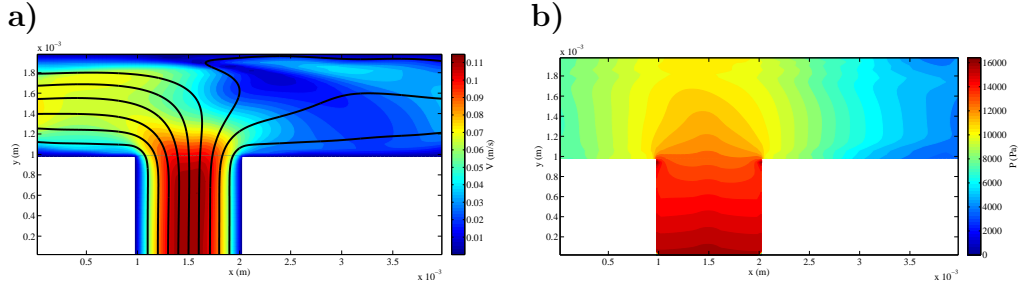


Figure 15: Numerical simulation performed upon the model (2.12) with Dirichlet boundary condition determined by using the reduced model approach. Mesh resolution : $100 \times 200 \times 50$. Inlet flow rate $Q_3 = 56.4 \mu L.s^{-1}$. On **a)**: velocity field and streamlines taken from a cut at $z = h/2$. On **b)**: cut at $z = h/2$ of the pressure field.

4.2.2. Direct numerical simulations

In this section we perform 3D numerical simulations on Equations (2.12). Instead of setting the velocity and stress profile at the outlet, we rather use the Neumann boundary condition (2.17)-(2.18), that stands for a free flow boundary condition. At the inlet, we use Dirichlet boundary conditions by setting a velocity profile computed with (2.16). As a consequence, the inlet flow rate Q_3 is prescribed.

The Figure 16 shows the results of the simulations taken at steady state for various inlet flow rates Q_3 . First, we notice on Figure 16 (on b, d, f) that, unlike previously (Figure 15), the pressure level at each outlet boundary $\Gamma_{1,2}$ is qualitatively the same. On Figure 16 (on a,c,e) we notice that the flow rate is much more important in the shortest branch than in the longest one which appears completely jammed.

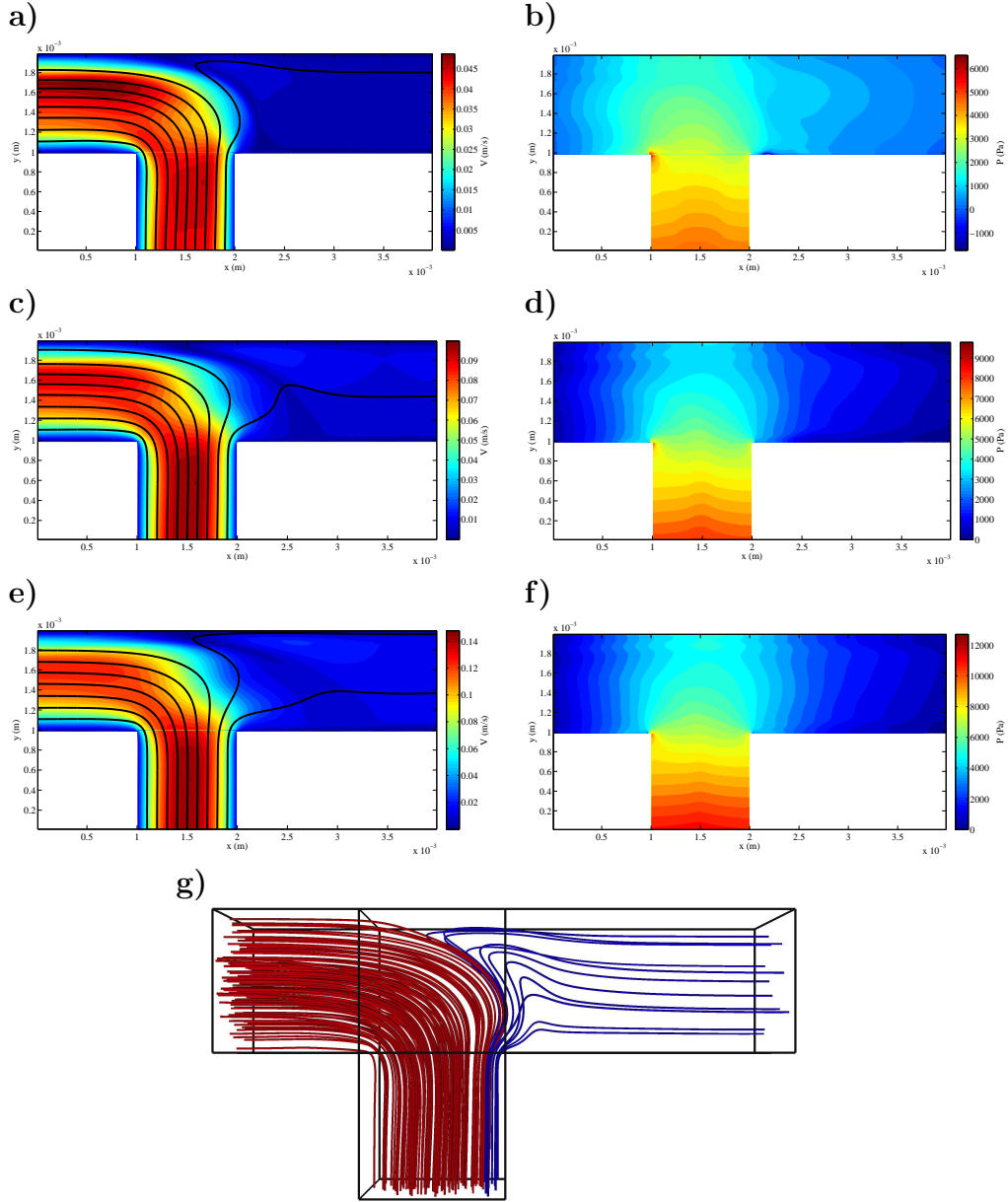


Figure 16: Numerical simulations performed upon the model (2.12), with the free boundary conditions (2.17)-(2.18). Mesh resolution: $100 \times 200 \times 50$. From top to bottom: $Q_3 = [25.28, 49.66, 72.04] \mu L.s^{-1}$. On **a**), **c**), **e**): velocity field and streamlines taken from a cut at $z = h/2$. On **b**), **d**), **f**): cut at $z = h/2$ of the pressure field. On **g**), 3D view of the streamlines computed from the velocities obtained in the most jammed case (**a**),**b**) ; in red: streamlines exiting through Γ_2 , in blue: streamlines exiting through Γ_1 .

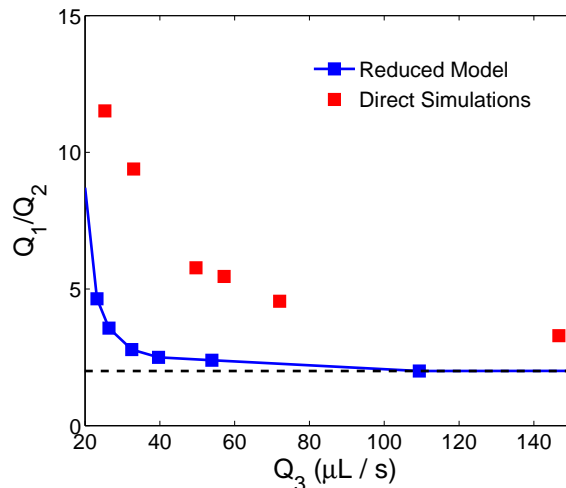


Figure 17: Ratio between the outlet flow rates Q_1/Q_2 as a function of the inlet flow rate Q_3 . Isolated squares: results computed from the direct simulations performed upon the full model (2.12). Squares and lines: results given by the reduced model. Dashed line: theoretical results for a newtonian fluid.

Let us now compare the outlet flow rate distribution given by the direct simulations with the results given in Section 4.2.1. We performed six numerical simulations on (2.12) for the following range of inlet flow rates: $Q_3 \in [25.28 ; 293.54] \mu\text{L} \cdot \text{s}^{-1}$. In each case, we let the system reach a steady-state. On Figure 17, the results given by direct numerical simulations are rather different from the predictions performed in Section 4.2.1. The numerical simulations (red dots) give outlet flow rates ratios Q_1/Q_2 that are in general higher than those predicted previously (blue dots). This difference might be due to some extensional effects of the flow of wormlike micelles at the middle of the junction.

In conclusion, we have seen that most of the time, the longest exit branch of the junction appears much more "jammed" here than when dealing with Newtonian fluid. Moreover, simple arguments are not sufficient to explain this fact completely, and 3D numerical simulation on the full model seems necessary. All these results can be seen as a first step for the study of wormlike micelles flows in porous media. Indeed, as stated in the introduction, porous media can be seen as a very inhomogeneous network of micro-channels. In this matter, we investigate in the next section the role of the asymmetry of

a junction.

4.3. *Flows in an weakly asymmetric junction : $\frac{L_2}{L_1} \sim 1$*

Let us consider a similar geometry as described on Figure 11. We now prescribe different lengths for the exit branches of the junction: we set $L_1 = 1mm$ and L_2 such that:

$$L_2 = L_1 (1 + \varepsilon).$$

Here $\varepsilon < 1$ is a dimensionless parameter that sets the asymmetry of the microfluidic junction. In the same way as before we prescribe the inlet velocity by using the Poiseuille-like model (2.16) and we use the Neumann boundary condition (2.17)-(2.18) at the outlet. The inlet flow rate is: $Q_3 = 25.28 \mu L.s^{-1}$. Again, by performing numerical simulations upon the model for different values of the asymmetry parameter $\varepsilon = [0.025, 0.05, 0.1, 0.2, 0.3]$ one can determine the influence of this asymmetry upon the outlet flow rate distribution.

The Figure 18 shows that the flow rate asymmetry is very sensitive to the channel asymmetry. For instance, even if we consider a very small asymmetry junction (that is $\varepsilon = 0.025$), the flow rate in the shortest branch Q_1 is 1.5 as big as the flow rate in the longest branch Q_2 (see Figure 19, a) and b).

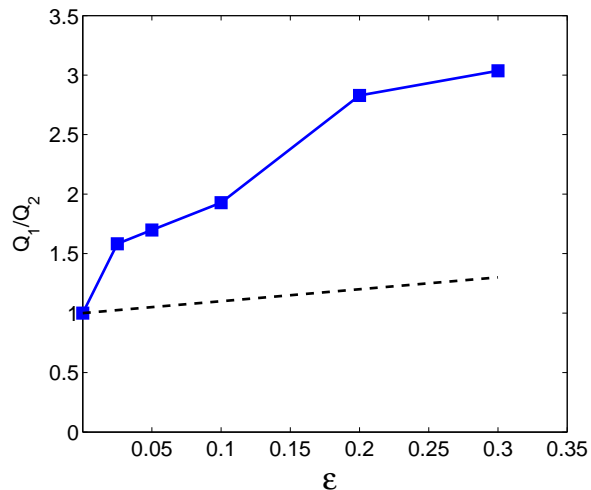


Figure 18: Ratio between the outlet flow rates Q_1/Q_2 as a function of the asymmetry ϵ of the exit branches. Squares: result given by performing direct numerical simulations upon the model (2.12) with free flow boundary conditions. Dashed line: theoretical result for a newtonian fluid.

As a consequence, if we consider the flow of a wormlike micellar solution in a micro-fluidic network that allows some small heterogeneity, a preferential path will be chosen by the fluid. In the case of a porous media, where the heterogeneity of the geometry is rather important, the choice of a preferential path should be even more important. This could be a problem for the use of wormlike micelles in enhanced oil recovery. The fact that an important fraction of the porous media containing the oil remains jammed could reduce the expected enhanced recovery rate. Moreover, the locations of the main/jammed paths should be difficult to predict since we have no control upon the microscopic heterogeneity.

5. Conclusion

A complete framework for 3D numerical simulations of non-newtonian fluids has been described in this paper. The particular case of flows through junctions was investigated. A modified version of the well known Johnson-Segalman's model has been used as a constitutive equation, as described in Section 2.1. This modified model ensures the normal stress to remain

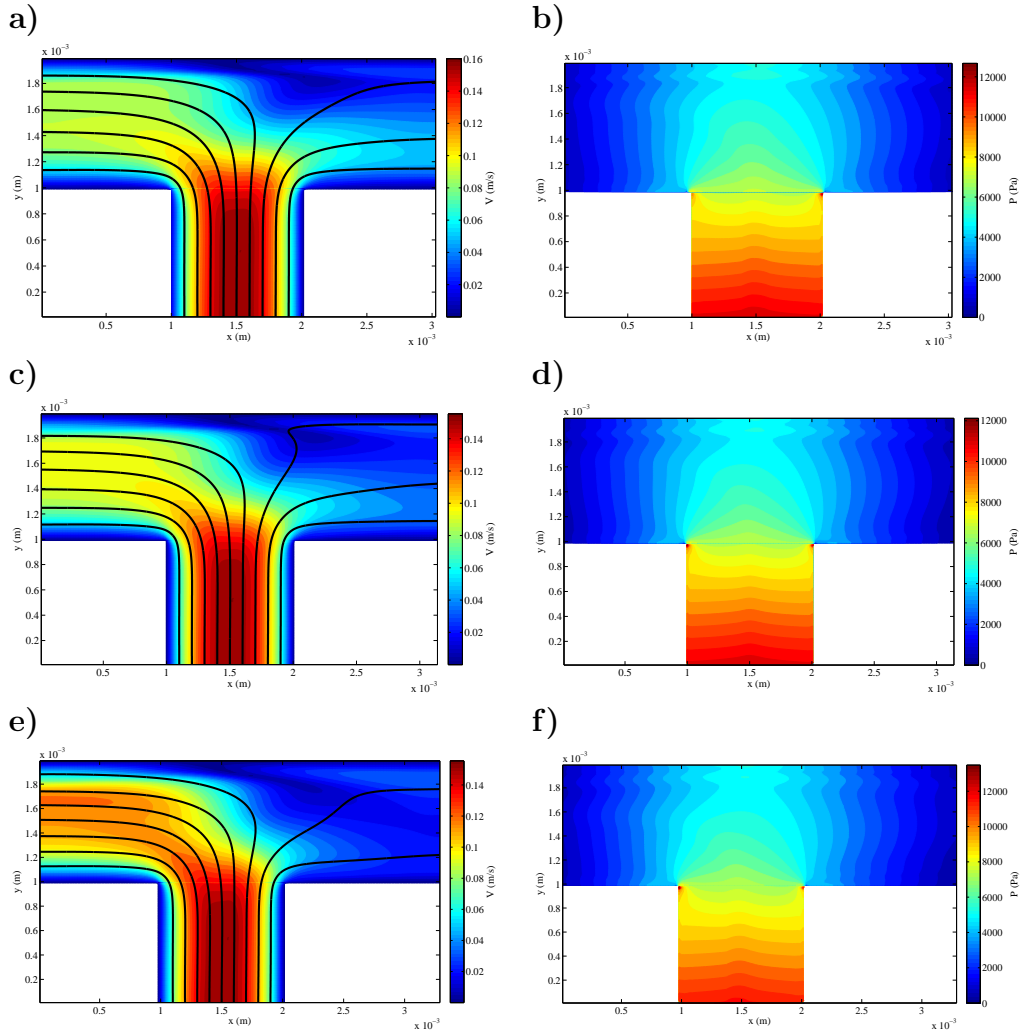


Figure 19: Numerical simulations performed upon the model (2.12), with the free boundary conditions (2.17)-(2.18). Mesh resolution: $100 \times 200 \times 50$. From top to bottom: $\varepsilon = [0.025, 0.1, 0.2, 0.3]$. On **a**), **c**), **e**): velocity field and streamlines taken from a cut at $z = h/2$. On **b**), **d**), **f**): cut at $z = h/2$ of the pressure field.

bounded in the situation of extensional flows. This problem happens often when dealing with pipe flows in junctions, as confirmed in Section 4.1.

Some issues concerning the inflow/outflow conditions have been widely studied here. Because of the very particular velocity profiles that appear when dealing with the Johnson-Segalman's model (see fig. 6), simple Poiseuille profiles based on newtonian rheology for inlet cannot be satisfactory here. In Section 2.1.3, we derived a non-newtonian Poiseuille-like model from the model described in 2.1. The stationary numerical solution of this Poiseuille-like model have been used as inlet conditions in latter simulations. Among other advantages, this novel inlet condition allows us to reduce the length of the inlet channel, usually needed to get an established flow at the junction.

Numerical simulations have been performed in a three dimensional context in section 4. These simulations have shown the jamming effect, which is a purely non-newtonian phenomenon, triggered by the geometry of the junction. Comparisons with a reduced hydraulic model have shown that full 3D simulations are necessary here.

Some improvements, in particular concerning the numerical scheme described in Section 3 may be conducted in the future, allowing the use of models for which the so-called "solvent viscosity" η is small, which is forbidden here (see Section 3.4).

- [1] J.M. Adams, S.M. Fielding, P.D. Olmsted, "*The interplay between boundary conditions and flow geometries in shear banding : Hysteresis, band configurations and surface transitions*", Journal of Non-Newtonian Fluid Mechanics, 2008.
- [2] P. Angot, "*A unified fictitious domain for general embedded boundary conditions*", Comptes Rendus en Mathématiques de l'Académie des Sciences, 2005.
- [3] F. Boyer, L. Chupin, P. Fabrie, "*Numerical study of viscoelastic mixtures through a Cahn-Hilliard flow model*", European Journal of Mechanics B, 2004.
- [4] F. Boyer, P. Fabrie, *Eléments d'analyse pour l'étude de quelques modèles d'écoulements de fluides visqueux incompressibles*, Springer, 2006.
- [5] M.E. Cates, S.M. Fielding, "*Rheology of Giant Micelles*", Advances in Physics, 2006.

- [6] M.E. Cates, "*Reptation of Living Polymers: Dynamics of Entangled Polymers in the Presence of Reversible Chain-Scission Reactions*", Macromolecules, 1987.
- [7] M. Cromer, L.P. Cook, G.H. McKinley, "*Pressure-driven flow of wormlike micellar solutions in rectilinear microchannels*", Journal of Non-Newtonian Fluid Mechanics, 2011.
- [8] A.W. El-Kareh, L.G. Leal, "*Existence of solutions for all Deborah numbers a non-Newtonian model modified to include diffusion*", Journal of Non-Newtonian Fluid Mechanics, 1989.
- [9] P. Español, X.F. Yuan, R.C. Ball, "*Shear banding flow in the Johnson-Segalman Fluid*", Journal of Non-Newtonian Fluid Mechanics, 1996.
- [10] Y. Fan, R.I. Tanner, N. Phan-Thien, "*Galerkin/least-square finite element methods for steady viscoelastic flows*", Journal of Non-Newtonian Fluid Mechanics, 1999.
- [11] R. Fattal, R. Kupferman, "*Time-dependent simulation of viscoelastic flows at high Weissenberg number using the log-conformation representation*", Journal of Non-Newtonian Fluid Mechanics, 2005.
- [12] H. Giesekus, "*A simple constitutive equation for polymer fluids based on the concept of deformation-dependent tensorial mobility*", Journal of Non-Newtonian Fluid Mechanics, 1982.
- [13] M.W. Johnson, D. Segalman, "*A model for viscoelastic fluid behavior which allows non-affine deformation*", Journal of Non-Newtonian Fluid Mechanics, 1976.
- [14] S. Kefi, J. Lee, T. Pope, P. Sullivan, E. Nelson, A. Hernandez, T. Olsen, M. Palar, B. Power, A. Roy, A. Wilson, A. Twynam, "*Expanding applications for viscoelastic surfactants*", Oilfield Review, 2004.
- [15] X.-D. Liu, S. Osher, T. Chan, "*Weighted Essentially Non-Oscillatory schemes*", Journal of Computational Physics, 1994.
- [16] C. Masselon, J.-B. Salmon, A. Colin, "*Nonlocal Effects in Flows of Wormlike Micellar Solutions*", Physical Review Letters, 2008.

- [17] C. Masselon, "*Effets non locaux dans un écoulement microfluidique de micelles géantes*", Phd Thesis at Université Bordeaux 1, 2008.
- [18] E. Miller, J.P. Rothstein, "*Transient evolution of shear banding in worm-like micelles solutions*", Journal of Non-Newtonian Fluid Mechanics, 2007.
- [19] P.D. Olmsted, O. Radulescu, C.-Y. David Lu, "*The Johnson-Segalman model with a diffusion term in a cylindrical Couette flow*", Journal of Rheology, 2000.
- [20] R.G. Owens, T.N. Phillips, "*Computational Rheology*", Imperial College Press, 2002.
- [21] C. Peskin, "*Numerical analysis of blood flow in the heart*", Journal of Computational Physics, 1977.
- [22] T.N. Phillips, A.J. Williams "*Comparison of creeping and inertial flow of an Oldroyd B fluid through planar and axisymmetric contraction*", Journal of Non-Newtonian Fluid Mechanics, 2001.
- [23] I. Ramière, P. Angot, M. Belliard, "*A fictitious domain approach with spread interface for elliptic problems with general boundary conditions*", Computer Methods in Applied Mechanics and Engineering, 2007.
- [24] T. Sochi, "*Single-Phase Flow of Non-Newtonian Fluids in Porous Media*", Journal of Polymer Science Part B: Polymer Physics, 2009.
- [25] H. Uzawa, "*Iterative Methods for Concave Programming*", Studies in Linear and Non-Linear Programming, 1958.
- [26] L. Zhou, P.A. Vasquez, P. Cook, "*Modeling the inhomogeneous response and formation of shear bands in steady and transient flows of entangled liquids*" Journal of rheology, 2008.